# Continuous–Wave NMR Imaging in the Solid State

***Andrew J. Fagan [1, 2], David J. Lurie [1]****

[1] Department of Bio-Medical Physics and Bio-Engineering, University of Aberdeen, Foresterhill, Aberdeen AB25 2ZD, U.K.

[2] Current address: 7T MR Facility, Wellcome Surgical Institute, University of Glasgow, Garscube Estate, Bearsden Road, Glasgow G61 1QH, UK.

* Corresponding author (telephone: + 44 1224 554061, email: d.lurie@biomed.abdn.ac.uk

## Abstract

A novel NMR technique for imaging materials exhibiting extremely short $T_2$ relaxation times is described and some examples of its application to materials of scientific and industrial interest are presented. The technique employs continuous wave (CW) radiofrequency irradiation of the sample together with continual detection, and thus the experimental deadtime inherent in pulsed techniques is effectively eliminated. The mechanisms which broaden the NMR linewidths of materials in the solid state and liquids in confined geometries are described, and the resulting difficulties which these broad linewidths pose to NMR imaging are outlined. A brief review of existing NMR imaging techniques is then presented. The CW-NMR approach to imaging is expounded, and the CW-NMRI system is described in detail. 1-D and 2-D images of the ingress of water ($^{1}$H imaging) and brine ($^{23}$Na imaging) into various cementitious materials are presented, together with images of the solid $^{27}$Al phase of a high-temperature refractory cement. The inter- and self-diffusion coefficients of a clay mineral, bentonite, were successfully measured, and the 2-D and 3-D imaging performance of the system was demonstrated on phantoms of poly(methyl methacrylate) (PMMA, Perspex / Plexiglas).

# Table of Contents

# 1. Introduction

The development of nuclear magnetic resonance (NMR) imaging techniques has traditionally focussed on imaging in the liquid state, in particular imaging the free water distribution in biological tissues. This has led to numerous important applications, culminating in the revolution in diagnostic imaging capabilities made possible with the introduction of whole-body MRI scanners into hospitals in the 1980s. Developments in NMR imaging in the solid state have likewise received much attention since the first NMR experiments in the 1940s, however progress in this area has lagged considerably behind its medical counterpart. In solids, or solid-like materials where atomic motion is very restricted, the NMR lines are broad and spin-spin relaxation times, $T_2$, are short compared to those normally found in liquids. This presents a very severe problem for the application of imaging techniques to such materials [1-4].

The essential feature of an NMR imaging system is the ability to encode the spatial information in a time of the order of $T_2$. In liquids, $T_2$s are of the order 30 – 300 ms

(corresponding to linewidths in the range 1 – 10 Hz), which is long enough to enable images to be generated using commercially-available hardware. The situation is drastically different in solids: with linewidths ranging from 10 to 100 kHz, $T_2$ relaxation times of less than 30 μs are typical. This difference stems predominately from intranuclear line broadening mechanisms, which are averaged to zero in liquids by rapid random isotropic motion, but which are not averaged to zero in solids because the atoms are more rigidly bound within the structure. The application of NMR imaging techniques to the study of porous media poses additional challenges: the presence of paramagnetic impurities, susceptibility-induced field gradients and chemical shift anisotropies all result in enhanced relaxation and, hence, broader resonance lines. Furthermore, the presence of liquids in such confined geometries can lead to adsorption phenomena on internal pore surfaces which shorten relaxation values compared to those found in the bulk liquid, to the extent that solid imaging techniques are required.

The maximum achievable spatial resolution of an NMR image is directly proportional to both the $T_2$ of the material under investigation and the magnitude of the applied field gradients. Consequently, for a solid state imaging system to achieve the same resolution as a liquid state imaging system, the field gradients must be increased to compensate for the decreased $T_2$ values. For example, it is difficult to produce them over large sample volumes (> 10 $cm^3$), and to switch large field gradients within the time needed for some imaging experiments. A further problem with the use of large field gradients is that the receiver bandwidth must be increased to accommodate the spread in resonant frequencies, and therefore the signal to noise ratio (SNR), which scales with the square root of the receiver bandwidth, can be reduced by several

orders of magnitude in the resultant image. This illustrates the fundamental problem and the technical difficulties of dealing with much shortened timescales.

These problems can be overcome, to some degree, by decreasing the effective NMR linewidth of the sample using techniques which reduce the line-broadening mechanisms within the sample, so that lower strength field gradients may be used (called 'line-narrowing' techniques). This can be achieved by using a range of special multi-pulse radio-frequency (RF) irradiation methods [5-10] or by physically spinning the sample at the magic angle [11-13]. An alternative approach to solid state NMR imaging which has been exploited in several techniques involves the application of sufficiently large magnetic field gradients to produce spatial localisation on the resonant spins, thereby retaining the broad linewidths which contain useful information from the $T_2$ relaxation phenomenon which broaden the lines [14-18]. However, various practical and/or technical problems have limited the success of these varied approaches to NMR imaging in the solid state, and to date no one technique has emerged as an all-round gold standard.

The technique described in this paper utilises continuous-wave (CW) detection, originally developed for electron paramagnetic resonance (EPR) experiments but adapted here to the study of materials in the solid state by NMR. In EPR, materials with electron $T_2$ relaxation times less than 1 μs are typically encountered. The signal from the sample under investigation is detected by recording the change in the electrical characteristics of the RF resonator as the sample is swept through resonance by a time-varying magnetic field applied across the sample. Indeed, swept-field CW-NMR with magnetic field modulation and lock-in detection was ubiquitous in the

early years of NMR, being used to perform spectroscopy on solids as early as 1949 [19]. More recent applications of this method include the study of crystallinity in stretched [20] and plasticized [21] rubber. In 1974, Lauterbur *et al.* suggested that slow passage NMR together with magnetic field gradients might be useful for imaging substances with very short relaxation times [22]. However, it was not until 1996 that the first paper describing just such an approach to NMR imaging was published by Lurie *et al.* [23].

Solid state NMR imaging has many potential application areas. To date, NMR imaging of solids has revealed its potential to probe the porosity of ceramics, rocks and other heterogeneous systems [24,25], to give insight into chemical and physical changes in elastomers under stress and during the ageing process [15,26], and to study polymerisation reactions and local dynamics of elastomers below the transition temperature [27]. Techniques have been developed to study the drying mechanisms of thin, coating layers, such as those found in the application of paints and glues [28], to image the diffusion of liquids into solids [29,30], and to study the hydration and hardening of cement paste [31,32]. Biomedical materials such as bones, teeth and dental cement have also been studied using NMR techniques [33-35].

## 2. Line Broadening Mechanisms

The narrow linewidths of liquids allow one to observe weak spin interactions such as the indirect spin-spin (J) coupling and the isotropic chemical shift (δ). In the solid state, however, linewidths are broadened considerably by much stronger interactions, involving mainly the dipole-dipole interaction (typically 10 – 100 kHz), chemical-

shift anisotropy (~ 1 kHz), the quadrupole interaction (~ 250 kHz), and the effect of paramagnetic impurities. For these reasons the J and δ interactions are generally not observed in solids [2].

The Hamiltonian describing the energy of interaction of a solid in an NMR imaging experiment is given by:

$$H = H_{ext} + H_{int} \quad (1)$$

where $H_{ext}$ represents all external influences on the spin system (static field $B_0$, radio-frequency field $B_1$, and field gradients G), and $H_{int}$ represents interactions internal to the spin system (the direct nuclear dipole-dipole, chemical shift (both isotropic and anisotropic), quadrupole, and indirect spin-spin (J-coupling) interactions) [36]. The $H_{ext}$ term usually dominates the evolution of the spin system during periods of strong RF irradiation of the sample, whereas the $H_{int}$ term (together with the field gradient contribution to $H_{ext}$) dominates during periods of free precession, provided that the system is viewed in a frame rotating at the Larmor frequency of the spin under consideration. In general, the dipole-dipole and anisotropic chemical shift interactions dominate $H_{int}$ and thus are responsible for line broadening in solids. Quadrupolar interactions are only of concern in materials with nuclear spin $I > ½$, whereas the J-coupling interaction is generally too weak to be observed. Magnetic susceptibility-induced field gradients which vary with position in heterogeneous materials also influence the spin system, tending to further broaden the observed linewidths.

## 2.1 The Dipole-Dipole Interaction

The dipole-dipole interaction is the through-space coupling of one magnetic spin with the local field of its neighbours. The interaction depends on the magnitude and orientation of the magnetic moments, and also on the length and orientation of the vector describing their relative positions. The Hamiltonian describing the energy acquired by a nuclear magnetic moment $\boldsymbol{\mu_i} = \hbar\, \gamma\, \mathbf{I}_i$ (where the nuclear spin angular momentum operator $\mathbf{I}_i = I_{ix} + I_{iy} + I_{iz}$) when placed in the local fields generated by a collection of other nuclear spins $\Sigma\boldsymbol{\mu_j}$ can be written as

$$H_D = \frac{\mu_0 \hbar}{4\pi} \sum_{i<j} \gamma_i \gamma_j \left( \frac{\mathbf{I}_i \cdot \mathbf{I}_j}{r_{ij}^3} - \frac{3\left[\mathbf{I}_i \cdot \mathbf{r}_{ij}\right]\left[\mathbf{I}_j \cdot \mathbf{r}_{ij}\right]}{r_{ij}^5} \right) \qquad (2)$$

The situation with a pair of spins is illustrated in FIG. 1, where the static field $\mathbf{B}_0$ is along the z-axis. To first order and neglecting terms in the expansion of equation (2) which lead to a change in nuclear quantum numbers of 1 or 2 (i.e. $\Delta m = \pm 1$ and $\pm 2$ transitions), the effect of $H_D$ is to split the Zeeman levels into many closely spaced energy levels, thereby causing a distribution of resonant frequencies and consequently a broad line. Equation (2) has been simplified by the van Vleck formula [2]:

$$H_D = \frac{\mu_0 \hbar}{8\pi} \sum_{i<j} \frac{\gamma_i \gamma_j}{r_{ij}^3} \left(1 - 3\cos^2 \theta_{ij}\right)\left[3 I_{zi} I_{zj} - \mathbf{I}_i \mathbf{I}_j\right] \qquad (3)$$

One can see from equation (3) that the van Vleck dipolar Hamiltonian is the product of a spatial part and a spin part. In liquids, the rapid isotropic molecular tumbling motion, which occurs at frequencies well above the dipolar linewidth, averages the spatial part $(1 - 3\cos^2\theta_{ij})$ to zero, thus nulling the dipolar broadening. In solids, the spins are constrained to vibrate and rotate about their mean positions, resulting in an effective dipolar Hamiltonian which is generally non-zero, and consequently in broad

lines. The NMR lineshape is approximately Gaussian [37], in contrast to the Lorentzian line associated with liquids. The linewidth is characteristically of order [38]

$$\Delta f = \frac{\mu_0 \gamma^2 \hbar}{8 \pi^2 r^3} \tag{4}$$

for the homonuclear case, and with $r$ the nearest neighbour separation, and assuming an internuclear distance of 0.15 nm, this gives $\Delta f$ = 35 kHz.

## 2.2 The Chemical Shift Interaction

The chemical shift can be defined as the shielding interaction between the electron clouds and the nuclear spin angular momenta; it is isotropic in liquids but has rotational anisotropy in solids. The spin Hamiltonian describing the interaction is therefore tensorial in nature:

$$H_{CS} = - \mathbf{I} \cdot \mathbf{S} \cdot \mathbf{B}_0 = -\gamma \mathbf{I} \cdot \boldsymbol{\sigma} \cdot \mathbf{B}_o \tag{5}$$

where **S** is the shielding tensor and $\boldsymbol{\sigma}$ is the chemical-shift tensor.

Unlike the situation with the dipolar interaction, which averages to zero in liquids due to the rapid molecular tumbling motion, the isotropic rotation leaves a residual chemical shift Hamiltonian

$$H_{CS} = -\sigma_i \, \omega_0 \, I_z \tag{6}$$

where $\sigma_i$ is the isotopic chemical shift given by the diagonal sum $\frac{1}{3}(\sigma_{xx} + \sigma_{yy} + \sigma_{zz})$. For solids, the full chemical shift Hamiltonian is [37]

$$H_{CS} = - \sigma_i \, \omega_0 \, I_z - \tfrac{1}{2} ( 3 \cos^2 \beta - 1) (\sigma_{zz} - \sigma_i) \, \omega_0 \, I_z \tag{7}$$

where $\beta$ is the polar angle between the polarising field direction and the principle axis system of the chemical shift tensor. The additional term in equation (7) is the anisotropic chemical shift which contributes to line broadening in solids.

## 2.3 The Quadrupole Interaction

For nuclear spins with spin quantum number I > ½, the nuclear charge distribution about the centre of gravity of the nucleus is not spherically symmetric. This asymmetry in the nuclear charge distribution gives rise to an electric quadrupole moment, Q, which interacts with electric field gradients established by electrons surrounding the nucleus. Although this is an electrical interaction, it depends on the magnetic quantum number and so affects the NMR spectrum.

The quadrupole interaction Hamiltonian for a single spin is

$$H_Q = \mathbf{I_i} \cdot \mathbf{Q} \cdot \mathbf{I_i} \tag{8}$$

where

$$\mathbf{Q} = \frac{eQ}{2I(2I-1)\hbar}\mathbf{V} \tag{9}$$

and $Q$ is the nuclear quadrupole moment of spin-I and $\mathbf{V}$ is the electric field gradient (EFG) tensor. For the case of an axially symmetric EFG tensor, the secular part of the quadrupole Hamiltonian is given by [2]

$$H_Q = \frac{eQV_{33}}{8I(2I-1)}\left(3\cos^2\beta - 1\right)\left(3I_z^2 - I(I+1)\right) \tag{10}$$

## 2.4 Magnetic Susceptibility Effects

When applying solid imaging techniques to highly heterogeneous material systems, the heterogeneity of the diamagnetic susceptibility also contributes significantly to line broadening. Susceptibility broadening arises because a localised region with susceptibility different to the surroundings perturbs the applied magnetic field both in and around itself. The geometry of the heterogeneity and its orientation relative to $B_0$ influence the degree of perturbation of the field, with the largest effects occurring at boundaries and in high fields. This creates two problems: the first is image distortion arising from different nuclei experiencing different magnetic fields; the second is attenuation of the signal and hence line broadening arising from diffusion of nuclei across the susceptibility-induced field gradients.

The offset magnetic field outside a cylinder of radius $a$ and susceptibility $\chi_2$, which is embedded in a material of susceptibility $\chi_1$ and placed in a magnetic field of strength $B_0$ such that the long axis of the cylinder is orthogonal to the field, is given by

$$\Delta B = \frac{(\chi_2 - \chi_1)a^2 \cos 2\varphi}{2r^2} B_0 \qquad (11)$$

where $r$ is the distance from the cylinder axis and $\varphi$ is the angle between the vector $\boldsymbol{r}$ and $\boldsymbol{B}_0$. Taking the materials as air and water, the susceptibility difference is $-9 \times 10^{-6}$, so that for $^1$H NMR at $B_0$ = 7.05 T (the field strength used in our own experiments), the maximum field offset is 32 μT, equivalent to 1.36 kHz. Such offset fields give rise to gradients of the order of several hundred T/m in the vicinity of micron-sized cavities within porous materials. Diffusion through these field gradients attenuates the NMR signal at time $t$ by a factor $exp(-\gamma^2 G^2 Dt^3/3)$, where $G$ is the gradient and $D$ is the diffusion coefficient.

Paramagnetic impurities in samples such as concretes and rocks can be present at considerable concentrations and thus can also give rise to line broadening. This can happen in two ways [38]: (i) a magnetic nuclear – electron dipolar interaction, which provides an efficient relaxation mechanism due to the very large electron magnetic moment (compared to that of the nuclear moment) and (ii) short (contact) and long range electronic shielding, which leads to gradients in paramagnetic susceptibility across the sample, with similar (although larger) effects to that due to the diamagnetic contribution to susceptibility broadening.

## 3. Overview of solid imaging techniques

Detailed reviews of solid state imaging techniques have been presented previously (for example, see Jezzard *et al.* [2], Demco and Blumich [3,39], and Blumich [40]), and thus only a brief overview is given here. Although 'soft' solid materials such as elastomers exhibiting linewidths less than 3 kHz can be imaged using Fourier imaging on modern solid-state NMR imaging systems, more specialised techniques are required to image nuclei in rigid matter. In general, two imaging strategies have been adopted: either the gradient strength can be increased or the linewidth can be reduced. Techniques utilising the former approach include stray-field imaging (STRAFI), the use of strong oscillating gradients, single point imaging (SPI) using pure phase encoding, and multiple quantum (MQ) imaging. Techniques utilising the latter approach include magic angle spinning (MAS), magic-angle rotating-frame (MARF) imaging, imaging with multi-pulse line narrowing, and magic echo imaging. By way of comparison, while the large gradient techniques adopt a brute force approach to

overcome the broad linewidths present in solids, line narrowing techniques attempt to replicate the conditions existing in liquids which suppress many of the principal line broadening mechanisms. In effect, the spins in the solid are made to act as if they were undergoing rapid isotropic thermal motion by introducing, via external forces, a time-dependence into the effective Hamiltonian describing the system such that the spins sample all directions of spin space in turn. Indeed, this time-dependence can be introduced in the spatial and / or the spin parts of the van Vleck Hamiltonian given in equation (3).

## 3.1 Stray-Field Imaging (STRAFI)

The idea of using the large static field gradients present in the fringe field of solenoidal superconducting magnets to image solids was first expounded by Samoilenko *et al.* in 1988 [14]. By using such large field gradients, which typically measure 60 T/m for 9.4 T magnets, spatial resolutions of the order of 10 μm are achievable in materials with linewidths of the order of 30 kHz. The resultant broad spread in resonant frequencies, of the order of 25 MHz $cm^{-1}$ for $^{1}H$ nuclei, means that even for moderately sized samples, the RF pulses do not have sufficient bandwidth to encompass the entire range of resonant frequencies to allow for imaging of the entire length of the sample. Every RF pulse, shaped or not, will excite resonance in a thin slice perpendicular to the gradient direction, and because the gradient direction cannot be changed, the sample must be mechanically moved through the gradient in order to excite the next slice. In this way, a 1D profile of the sample is acquired in the direction of the gradient in a stepwise fashion. The measured magnetisation corresponds directly to the sample's spin density, and therefore no Fourier transformation of the data is required. Two- and three-dimensional image data sets

can be acquired by combining sample rotation and translation, with image reconstruction of a sufficient number of profiles performed by using back projection. However, mechanical complexities and time constraints associated with such sample manipulations have rendered STRAFI a predominately 1-D imaging technique, with experimental set-up typically optimised to this end [38].

Several variations of the original STRAFI method have been reported. Frequency-swept experiments, in which the NMR spectrometer frequency was swept such that the sensitive slice moved through the sample, have been carried out on sufficiently thin samples [28]. Another variation was reported by Mallett *et al.*, who used a magnetic field sweep facility to move the sensitive slice through the sample [41]. These experiments eliminated problems associated with positional reproducibility and backlash or misalignment in the sample travel. For 3-D imaging of samples which could not be rotated and for which high resolution was only required in one dimension (e.g. initially wet planar coatings of paint and varnish), Godward *et al.* developed a system which uses STRAFI in conjunction with pulsed orthogonal gradients [42]. The realisation that the use of a superconducting solenoid magnet with a very high central field homogeneity is not necessary for STRAFI has led to the development of two magnet designs specifically targeted to STRAFI work. The first is the NMR-MOUSE, a portable magnet and spectrometer system developed by Blumich *et al.* [43,44]. This system uses an asymmetrical permanent magnet producing a field of 0.41 T and an RF coil placed between the magnet pole pieces with its axis perpendicular to the surface of the magnet. The stray field outside the magnet has a maximum field gradient of 14 T/m, and can be used to probe to depths of several mm. The second example is a novel high-gradient permanent magnet designed for the

profiling of planar films and coatings by Glover *et al*. (GARField) [45]. This magnet provides a typical operating field of 0.8 T with a homogeneous gradient of 20 T/m within a useable interpole access of 20 mm.

## 3.2 Imaging with Oscillating Gradients

The oscillating gradients technique uses the same brute force approach as STRAFI, i.e. applying large gradients to overcome the broad linewidths in order to acquire an image with good spatial resolution. In STRAFI, the radiofrequency pulses are necessarily applied in the presence of the gradient, which leads to ill-defined excitation slices within the sample. However, it is often desirable to irradiate the sample with no applied gradient, and then to observe the signal in the presence of a gradient. The difficulty here is to switch the large gradients and allow them to settle in a timescale short compared to the $T_2^*$ of the sample. A solution to this problem was demonstrated by Cottrell *et al.* in 1990 [16], who used a sinusoidal variation in order to apply a rapidly varying time-dependent gradient. The power required for the application of large gradients was reduced by making the gradient coils part of a tuned circuit. Furthermore, they applied the initial 90° RF pulse at a zero crossing of a sinusoid, so that the RF power requirement was simply that associated with a solid.

A typical timing diagram used in this experiment is outlined in FIG. 2. The first half-cycle of the field gradient after the 90° pulse encodes the spatial information on the FID. The gradient is then reversed in the second half-cycle with a gradient echo forming after one period of the gradient oscillation. Provided that $2\tau < T_2^*$ further gradient echoes will continue to form at times $2n\tau$, the amplitudes decreasing

successively as determined by $T_2^*$. A suitable choice of gradient permits the echo formation clear of the 90° pulse dead-time and there is no 180° pulse to further obscure the signal. Schemes for 2-D [46] and 3-D [47] imaging were subsequently developed, the latter employing doubly resonant gradient coils to allow for imaging using standard 3DFT techniques.

Although the inclusion of the gradient coils into a resonant circuit allows an increase in the gradient strength (typically 1 - 10 T/m), it is still significantly lower than that used in STRAFI. Furthermore, technical limitations on the oscillation period ($TE_{min} \sim 200$ μs) limit the shortest measurable relaxation time [16]. Hence the oscillating gradient scheme has proved to be suitable for imaging soft solids (rubber and soft polymers) with linewidths of up to 3 kHz [48,49], although the technique has been used in combination with multi-pulse line narrowing techniques to extend the range of applications to stronger dipolar solids [50].

## 3.3 Single Point Imaging (SPI)

Single point imaging was first suggested by Emid in 1985 [51] as a method for minimising the effect of all line broadening mechanisms while using modest gradient strengths. The evolution of the magnetisation in the gradient is detected by measuring only one data point of the FID at a fixed time τ after the excitation pulse. Because this time is fixed and the gradient strength is incremented between successive experiments, only the evolution of the spins due to the gradients is observed; the evolution due to dipolar interactions, chemical shifts and other line broadening

mechanisms is constant and therefore is not observed. The spatial resolution is only limited by the magnitude of the applied gradient.

The SPI technique tends to be very hard on the gradient amplifiers because of the need to use large gradients when imaging solids, but also because the time during which the gradients phase encode the signal is necessarily less than the $T_2^*$ of the sample under investigation, and hence rapid gradient switching is required. To alleviate this problem somewhat, the gradients are turned on and allowed to stabilise before applying the RF pulse. Consequently, the RF pulses are applied in the presence of a gradient, and therefore extremely short, broadband pulses are required in order to excite the full range of frequencies across the sample. Because only one point in *k*-space is acquired after each excitation, acquisition times tend to be very long, and therefore small flip angles are typically used in order to allow for the use of short $t_R$ values without saturation (subject to duty-cycle limitations of the gradient set). Several techniques aimed at reducing the image acquisition time of the basic SPI experiment have been described, including the turbo spin echo SPI technique of Beyea *et al.* [24], which obtained multiple phase encoded *k*-space data points with each RF excitation pulse train, and the multi-point *k*-space mapping techniques of Cho and Ro [52] and Fernandez-Seara *et al.* [53], which extend one phase encoding gradient in time, allowing for the acquisition of *n k*-space points per excitation.

Despite these improvements, the SPI technique is inherently slow and, furthermore, the intense, rapidly switched gradient pulses it uses can lead to excessive gradient vibration. The SPRITE (single point ramped imaging with $T_1$ enhancement) technique, developed by Balcom *et al.* in 1996, overcomes these problems and

enables the introduction of quantitative $T_1$ contrast into images [54]. Unlike the SPI sequence, the magnetic field gradients in the SPRITE sequence are not switched on / off for each acquisition. Instead, the primary phase encode gradient $G_z$ is ramped in equally-spaced discrete steps (typically 0.5 – 5 ms in duration), while conventional phase encoding gradients are applied in the secondary directions ($G_x$ and $G_y$). A broadband RF pulse with flip angle $\alpha$ is applied at each step of $G_z$, and a single data point is measured on each resulting FID after a time $t_p$. Gradient vibrations are reduced due to the lower *dB/dt* inherent in the technique. A marked time improvement is achieved with samples where $T_1$ relaxation times are on the order of the gradient rise time [55,56]. Gradient steps are typically limited to 0.5 – 5 ms in duration in order to remain within the duty cycle limits of the gradient amplifiers. $T_1$ contrast is introduced into the images by partial saturation of magnetisation components that have longitudinal relaxation times longer than the gradient switching time. Improvements to the sensitivity (both SNR and acquisition speed) of the basic SPRITE sequence using two centric scanning acquisition strategies have recently been described. The SPIRAL-SPRITE technique reported by Szomolanyi *et al.* [57] employs a spiral *k*-space scanning strategy, and is carried out by applying sinusoidally ramped X and Y gradients with a constant Z gradient. The Conical SPRITE technique reported by Halse *et al.* [58] employs a system of spiral trajectories mapped to a conical surface, with the X and Y gradients varied sinusoidally and the Z gradient stepped in a linear ramp.

## 3.4 Multiple Quantum (MQ) Imaging

An MQ coherence of order *p* can exist in a coupled spin system, and in a quadrupolar nucleus under certain conditions, when the system contains states |i> and |j> whose

magnetic quantum numbers differ by $M_i - M_j = \pm p$. In this case, the oscillation frequency due to such transitions is $p$ times larger than the Larmor frequency $\omega_0$. In general, NMR experiments detect single quantum coherences, i.e. $p = \pm 1$. Higher order coherences do not produce magnetic dipole radiation and thus cannot be detected directly by a conventional dipole antenna used to detect single-quantum resonances, and instead are detected by their influence on observable single quantum coherences [2]. Furthermore, although very high order coherences can be induced in dipolar solids, the intensity of the NMR signal decreases strongly with increasing $p$. The interest in MQ coherences for solid imaging arises because the rate of phase evolution of a multiple quantum coherence of order $p$ in a field gradient is enhanced by a factor $p$. This means that the frequency resolution is enhanced by a factor $p$, and thus one could conceivably obtain good spatial resolution in a broad linewidth material without the need to use very large gradients. Furthermore, MQ coherences in solids can be less sensitive to certain spin interactions, leading to narrower linewidths and potentially still better spatial resolution [40].

A typical MQ coherence imaging pulse sequence comprises four distinct steps: preparation, evolution, reconversion and detection. A range of multi-pulse sequences exist for exciting different order QM coherences during the preparation period (see [59,60]). The excited coherences then evolve for a time $t_1$ under the influence of the applied space encoding gradient to allow for imaging, before being reconverted to single quantum coherences and detected in the usual manner. Phase cycling schemes can also be used to extract different coherence orders. MQ imaging was first shown for dipolar coupled protons in adamantane by Garroway *et al.* in 1984 [17]. Coherences of order up to $p = 20$ were observed, although amplification of the effective gradient

strength was only achieved up to $p = 14$ due to the decrease in signal intensity as $p$ increased. The technique was later applied to spectroscopic deuteron solid state imaging, where deuterated polymers exhibiting linewidths of the order of 250 kHz were imaged with sub-millimetre resolution using double quantum coherences [61]. MQ techniques have also found use in conjunction with magic angle spinning (MAS) techniques [62-64], wherein the MQ coherences were used to improve spectral resolution, to suppress signals from isolated spins-½, and to estimate local molecular structure through internuclear distances and molecular torsion angles [65]. Furthermore, the possibility of exciting and detecting proton double quantum coherences in inhomogeneous static and radiofrequency magnetic fields was investigated by Wiesmath *et al.* [66] using the NMR MOUSE system.

## 3.5 Magic Angle Spinning (MAS) Imaging

Early work by Andrew [67] and Lowe [68] in 1959 demonstrated how the dipolar part of the interaction Hamiltonian could be averaged to zero by spinning the sample about the magic angle axis (54.74° to $\mathbf{B_0}$). However, this technique was not used in imaging experiments on solid materials until 1988, when Cory *et al.* successfully resolved two pieces of silicone rubber samples separated by 1 mm by rotating them at 2 kHz [11]. MAS is a line-narrowing technique which eliminates homonuclear and heteronuclear dipolar coupling, as well as chemical shift anisotropy, while retaining the isotropic chemical shift. It effectively averages to zero the spatial part of the van Vleck Hamiltonian in equation 3. However, the MAS rotation frequency must exceed the dipolar coupling strength for the dipolar contribution to be fully averaged, a condition which is seldom met for solid imaging since typical rotational frequencies are < 20 kHz [40]. A further problem is that spinning sidebands are observed if the spinning

frequency is smaller than the anisotropy of the interaction [1]. Nevertheless, MAS imaging is very suitable for imaging heterogeneous materials, since it conserves the isotropic chemical shift. In homogeneous materials, MAS techniques are often used in conjunction with other more efficient methods for homonuclear dipolar decoupling. The MAS technique has some drawbacks related to the existence of centrifugal forces ($10^5$ g typical) which can cause deformation, fracture and separation of materials, and to the restriction in the geometry (preferably axially symmetric samples are imaged) and size of the sample (~ 10 mm), together with technically demanding hardware.

Several approaches to imaging using MAS have been proposed, but the most extensively used experiments employ rotor-synchronised rotating gradients, in which the gradients are rotated synchronously with the spinning sample so that the gradients appear stationary in the sample frame [1]. Both frequency and phase encoding procedures have been used to generate images for $^1$H [12] and $^2$H [69]. When imaging rare nuclei like $^{13}$C, the signal can be enhanced by cross-polarisation from $^1$H to $^{13}$C, while the detection is done in the presence of high-power heteronuclear decoupling [70].

## 3.6 Magic Angle Rotating Frame (MARF) Imaging

Magic angle rotating frame imaging is another technique which uses the concept of a magic angle to produce line narrowing. This experiment, originally developed by Lee and Goldberg in 1965 [71], is based on the evolution of the spins around an effective radiofrequency field $\mathbf{B}_{\mathbf{eff}}$ tilted at the magic angle as seen in the rotating frame, while the sample remains static. It works on the spin part of the interaction Hamiltonian, averaging to zero bilinear interactions such as the dipolar interaction when $\vartheta$ is set to

the magic angle and reducing linear interactions such as the chemical shift anisotropy (which are scaled as $\cos \vartheta$). The MARF technique produces better dipolar decoupling compared to the MAS method, since the Hamiltonian modulation frequencies can be an order of magnitude higher with MARF. However, the SNR is intrinsically low, while the ability to produce the magic angle conditions at every point in the sample depends strongly on the precision and stability of field gradients applied across the sample, which can be difficult to achieve in practice at the required magnitudes [39].

The effective field $\mathbf{B_{eff}}$ is generated using a combination of a static field gradient $G_{0x}$ and an RF field gradient $G_{1x}$, both of which are applied in the laboratory frame along the $\boldsymbol{B_0}$ and $\boldsymbol{B_1}$ directions respectively and are needed to ensure that $\mathbf{B_{eff}}$ varies linearly in amplitude but at constant orientation. To maintain the orientation of the effective field at the magic angle at all positions in the sample, the gradient amplitudes must be set such that $G_{1x}/G_{0x} = \sqrt{2}$. This condition limits the resolution of the method because of the relatively low values of the radiofrequency field gradient which can be achieved experimentally.

Two detection schemes are possible. In the first scheme, used in the original Lee-Goldberg experiment [71], the signal is detected in the rotating frame after the application of a 90° RF detection pulse following the evolution for a variable time $t_1$ in the spin-lock $B_{eff}$ field at the magic angle [25]. A dephasing delay $t_d \gg T_2$ is used before applying the 90° pulse to remove any transverse magnetisation, and thus only the desired longitudinal magnetisation is measured. Single point detection is then used, while projections at different angles can be measured by gradient or sample rotation. The second is a direct detection scheme, first demonstrated by Medfed and

Atsarkin [72], which uses a spin-echo sequence to generate transverse magnetisation in the tilted rotating frame, precessing about the z' axis with frequency $\omega_{eff}$, which is in the audio frequency (AF) range. Therefore, a separate AF coil is required to generate the spin echo pulses, which is decoupled from the RF coil by aligning it along the z-axis in the laboratory frame. Mechanical oscillations in the AF coil in this direct detection scheme can be problematic. The former, indirect, detection method obviates the need for the audiofrequency channel, and although it is more time consuming and provides the same line narrowing, it nevertheless gives a higher SNR because the signal is detected in the rotating frame (i.e. higher excitation frequency used, $\omega_0$ compared to $\omega_{eff}$). Several improvements have been made to the basic indirect MARF technique over the past few years, resulting in $T_2$ [25], $T_{1\rho}$ [73] and $T_{2\rho}$ [74] weighted contrast in images of various polymers.

## 3.7 Imaging with Multi-Pulse Line Narrowing

Multiple pulse (MP) sequences work on the spin part of the interaction Hamiltonian, and are based on the original ideas of Ostroff and Waugh [75] and Mansfield and Ware [76] of extending the time domain signal of dipolar coupled systems by applying a cyclic train of 90° pulses. An MP sequence typically consists of a train of several hundred RF pulses comprising repeated sets of $n$ pulses [2], with $4 \leq n \leq 48$. If the sequence is applied at a rate sufficiently rapid compared with the value of the linewidth to be narrowed, it will average to zero dipolar interactions within the sample, while the chemical shift interaction is either scaled or eliminated, depending on the type of MP sequence used.

Solid imaging using MP sequences involves difficult experimental set-up and is very demanding of the hardware, requiring high-powered pulses with excellent phase and amplitude stability. The free induction decay signal is sampled between pulses, and hence the overall efficiency of the sequence depends on the quality of the RF pulses. Furthermore, low quality-factor RF coils must be used to allow for the generation of RF pulses with the required short rise and fall times, which reduces the sensitivity and hence the spatial resolution. These issues, among others, have limited the widespread use of MP sequences for solid imaging. The first MP sequence was the WAHUHA sequence developed by Waugh *et al.* in 1968 [77]. Many of the pulse sequences developed since then have been based around this one, with various modifications aimed at improving the spatial resolution. Examples include the MREV-8 sequence developed by Mansfield in 1971 [78] and the BR-24 sequence developed by Burum and Rhim in 1979 [79]. Indeed, a form of the MREV-8 sequence was used in the first paper in which MP line narrowing was applied to imaging in 1975 [80] (1D profiling), and also the first 2-D image in 1985 [5].

The space-encoding gradients need to be introduced into the MP sequence in such a way that they do not influence the line-narrowing efficiency of the sequence. The approach used with the MREV-8 sequence is to apply the RF pulses in the presence of static field gradients, allowing for the introduction of $T_1$ or $T_{1\rho}$ contrast into the images by storing the magnetisation along $B_0$ (Zeeman storage) or $B_1$ (spin-locking) respectively [5]. However, the spin evolution under the influence of the gradients which invariably results from this approach leads to non-uniform resolution across the image, and a balance must therefore be struck between gradient strength and offset dependence for optimising the spatial resolution. An improvement in dipolar

decoupling efficiency and image resolution is obtained when oscillating rather than continuous gradients are used. Off-resonance effects can be minimised if the RF pulses are applied at the zero crossings of the gradients, although problems with non-uniform spatial resolution still exist. However, second-averaging techniques have been used to eliminate the phase shifts in the rotating frame causing the off-resonance effects [6,81].

The best spatial resolution is obtained when ultrashort (2 - 5 μs) gradient pulses are applied in the windows of a time suspension (i.e. all interactions are suppressed) MP sequence incorporating second-averaging techniques [82], albeit at the expense of demanding gradient hardware. Yet another variation is the combination of MP and MAS techniques, resulting in a combined rotation and multiple-pulse spectroscopy (CRAMPS) experiment, first implemented by Cory *et al.* in 1988 [83] and later extended to incorporate the magic echo-based sequence TREV-8 [84,85]. The advantage of such an approach is that the large dipole interaction can be removed by the MP sequence, while the chemical shift anisotropy broadening can be removed by MAS (pulse techniques alone cannot be used to separate the contributions of isotropic and anisotropic chemical shifts, so both are removed or both are preserved).

## 3.8 Magic Echo Imaging

The line-narrowing techniques discussed thus far only work effectively for isolated coupled spin pairs; if more than two spins couple, refocusing of the homonuclear dipole-dipole interaction is incomplete. Complete refocusing can, however, be done in these situations using the magic echo, even after a time as long as $T_2$, which allows more time for gradient switching, which in turn significantly improves the spatial

encoding potential with rigid solids [10]. The dipole-dipole interaction scales with the second Legendre polynomial $P_2(\cos\theta) = \frac{1}{2}(3\cos^2\theta - 1)$ (cf. equation 3), and thus $P_2 = (1 \text{ or } -\frac{1}{2})$ for $\theta = (0° \text{ or } 90°)$ respectively. Therefore, complete refocusing occurs if the spin system evolves for a time [$2\tau$ under $\theta = 0°$ *and* $4\tau$ under $\theta = 90°$].

The most successful magic-echo scheme that has been developed for imaging experiments is the magic-sandwich echo (MSE) sequence, first reported by Rhim *et al.* in 1971 [86]. This original MSE pulse sequence consisted of many $n180°_x$ and $n180°_y$ pulses sandwiched by $90°_y$ and $90°_{-y}$ pulses, illustrated in FIG. 3(a). The sign of the homonuclear dipolar Hamiltonian is reversed during the sandwich period of RF irradiation, resulting in a negative dipolar evolution with the strength of the dipole coupling reduced by a factor of 2. By setting the duration of this negative evolution equal to $4\tau$, where $\tau$ is the initial positive evolution period, an echo occurs at $6\tau$, in the absence of any RF field. The requirement of using $n180°$ pulses can be removed by using instead two continuous RF irradiations with reversed phases (FIG. 3 (b)) [8].

Two approaches to spatial encoding exist: frequency encoding using time suspension MP sequences incorporating magic echoes, similar to the MP sequences using solid echoes discussed in the previous section; and using pure phase encoding. The first approach uses stroboscopic measurement of multiple magic echoes, with spatial encoding performed by gradient pulses of constant strength applied in the windows of the multiple-MSE pulse sequence [9]. The free-evolution windows are long compared to solid echo-based MP sequences, so gradient switching is comparatively easy. The second approach uses the same principles as single point imaging discussed earlier: because the echo time and the gradient-pulse time are kept constant, the spin system

only evolves under the influence of the variable gradient amplitude (ignoring transverse relaxation effects). This magic echo phase encoding imaging (MEPSI) experiment was first reported by Hafner *et al.* in 1991, and later extended to 3-D imaging with the addition of a third phase-encoding gradient, with a consequently large increase in image acquisition time [87].

## 3.9 Continuous Wave NMR Imaging (CW-NMRI)

Despite the range of techniques that have been developed to image materials in the solid state, no one technique has emerged as an all-round gold standard. STRAFI is an inherently 1-D technique, and has consequently found application predominately in imaging materials where the process of interest has been reduced to 1-D, e.g. profiling perpendicular to thin films, where high resolution imaging of the in-plane processes are not so critical. The SPI/SPRITE technique, while perhaps the most successful technique to date from the point of view of its range of applications reported in the literature, like the STRAFI technique imposes a lower limit on the shortest $T_2$ value which can be studied. Line-narrowing techniques, by their very nature, lose useful information from the $T_2$ relaxation phenomena that broaden the lines, often require the application of high RF power, and place restrictions on sample size. Together with the complexity of the experimental set-up and the severe instrumentation requirements, their application to the imaging of solid materials has been limited.

An alternative approach to solid imaging is the continuous-wave NMR imaging (CW-NMRI) technique, which uses continuous RF irradiation and detection in the presence

of continuously-applied, moderately strong gradients. This technique offers a number of advantages compared to other solid imaging techniques:

- The use of CW RF irradiation and detection eliminates the equipment dead time inherent in all other techniques, thus effectively removing the limit on the shortest value of $T_2$ that can be investigated;
- The problems associated with rapid gradient switching are avoided through the use of continuously-applied gradients;
- The use of magnetic field modulation together with phase-sensitive detection using a lock-in amplifier renders CW-NMRI an extremely narrow-bandwidth detection technique, and thus the penalty inherent in all other techniques of a reduced SNR with increasing gradient strength (due to the increased frequency bandwidth) is removed;
- The RF power requirement in CW-NMRI is a factor of $10^3$-$10^6$ lower compared to the other solid imaging techniques, thus making it practicable to envisage examination of full-size structural components which might prove problematic for conventional pulsed techniques due to excessive RF power requirements.

A prototype system capable of producing 2-D images of rigid polymers has been described previously [88], while an upgraded system was used to study a range of heterogeneous materials such as cements and rocks [89].

# 4. CW-NMR Imaging

## 4.1 CW-NMR Spectroscopy

In the CW-NMR experiment, the magnetic field $B_0$ is swept slowly through resonance by the application of a ramped, offset magnetic field while the sample is continually irradiated at a fixed frequency [23,88,89]. The steady-state solutions to the Bloch equations (see [36], for example) are valid in this experiment provided the magnetic field sweep is sufficiently slow (the 'slow passage' condition), i.e. provided that equilibrium is maintained between the radiofrequency field and the nuclear magnetisation. If the resonance is traversed too rapidly, the magnetisation becomes saturated and consequently the measured signal diminishes. The slow passage condition is satisfied when

$$\frac{dB_0}{dt} \ll \gamma(\Delta B_{1/2})^2 \qquad (12)$$

where $\Delta B_{1/2}$ is the linewidth in field units. Typically, field sweep rates of the order of $1.6 \times 10^{-2}$ Ts$^{-1}$ are used, well below $\gamma(\Delta B_{1/2})^2 \sim 1$ to $10^3$ Ts$^{-1}$ which is typical for the solid materials studied by the CW-NMRI system [89,90].

To understand the CW-NMRI experiment, it is useful to consider the basic CW-NMR spectrometer illustrated schematically in FIG. 4. With a sample placed in a resonator located in a magnetic field, a signal from a radiofrequency source is applied to one of the terminals of a hybrid junction. This device serves to split an input signal into two, with each component following a different path to the output terminal where they are recombined. When the resonator is matched to 50 Ω, the incident RF power is equally split between the resonator and the 50 Ω load, and no signal appears at the

output terminal. The magnetic field applied across the sample is then swept using a time-varying ramped magnetic field and at resonance the spins absorb energy, which changes the impedance of the resonator and leads to an impedance mismatch across the hybrid junction. This mismatch causes power to be transmitted through the junction to its output terminal, where it is passed to the detector. A plot of detector output versus magnetic field would therefore show the sample's magnetic resonance absorption spectrum.

A diode detector is used to rectify and smooth the RF power to a DC voltage. The change in signal as resonance is achieved is often very small (~ 10 μV) compared to the electrical noise present in the system, and therefore an audiofrequency modulation is superimposed on the ramped magnetic field, with lock-in detection used to extract the signal with the same frequency as the modulation and at a fixed relative phase. This 'phase-sensitive' detection by a lock-in amplifier essentially represents a very narrow bandwidth detection scheme, and since the detected noise scales with the square root of the bandwidth, there is a resultant large increase in the measured signal-to-noise ratio (SNR) using magnetic field modulation techniques. The output from the lock-in amplifier is proportional to the change in signal reflected from the resonator as the field is swept, i.e. it is the first derivative of the absorption mode signal.

## 4.2 Magnetic Field Modulation

With the magnetic field modulation superimposed on the ramped magnetic field, the time-dependent magnetic field experienced by the sample can be expressed as

$$B(t) = B_0 + B_{ramp} + B_{mod}$$

$$= B_0 + \Delta B_0 \, (t/t_0 - ½) + ½B_m \sin \omega_m t \qquad (13)$$

where:

$B_{ramp}$ is the ramped field and is $= \Delta B_0 \, (t/t_0 - ½)$;

$B_{mod}$ is the sinusoidal modulation field with amplitude $½B_m$;

$\omega_m$ is the modulation frequency; and

the magnetic field $(B_0 + B_{ramp})$ is swept over the range $\Delta B_0$ from $(B_0 - ½\Delta B_0)$ to $(B_0 + ½\Delta B_0)$.

To satisfy slow passage conditions, $\omega_m$ must be sufficiently small such that there are several cycles of the modulation frequency during the passage between the half-amplitude points of the resonance line, i.e.

$$\omega_m \ll \gamma \, \Delta B_{½} \qquad (14)$$

Under these conditions, the magnetic field $(B_0 + B_{ramp})$ can be considered to be effectively constant. The mechanism whereby the magnetic field modulation is transformed to RF power modulation is illustrated in FIG. 5. The field modulated sine wave $\sin \omega_m t$ is converted by the nonlinear lineshape to a complex signal $S(B)$ that is a superposition of the fundamental modulation frequency $\omega_m$ and a large number of harmonics of $\omega_m$:

$$S(B) = \sum_{n=0}^{\infty} \left[ a_n(B) \cos n\omega_m t + b_n(B) \sin n\omega_m t \right] \qquad (15)$$

The measured signals deriving from different points on the resonance line shown in FIG. 5 are composed of different combinations of the fundamental and harmonic terms in the Fourier series expansion of equation (15). Thus the signal from the

inflection point C on the resonant curve in FIG. 5 is composed primarily of the fundamental $sin\ \omega_m t$, while that at the centre point A is composed primarily of the second harmonic $cos\ 2\omega_m t$. The signal from points B and D contain the fundamental, second and higher harmonics in the Fourier series, but are inverted and phase shifted with respect to each other. Likewise, signals from corresponding points on different sides of the curve are phase shifted by 180° with respect to each other. By way of illustration, the signal arriving at the detector is illustrated in FIG. 6(a) with no field modulation and FIG. 6(b) with field modulation, where $S_1$ represents the signal amplitude resulting from the $B_1$ field at frequency $\omega_0$, while $S_m$ represents the amplitude of the modulation envelope at frequency $\omega_m$, In the situation depicted in FIG. 6(b), the RF frequency $\omega_0$ is modulated primarily by the fundamental $sin\ \omega_m t$ term of equation (15), which occurs for signals deriving from points C and C′ in FIG. 5. The detector strips off the RF component and passes the audiofrequency envelope component to the lock-in amplifier.

The use of magnetic field modulation with lock-in detection influences the measured shape and amplitude of the absorption spectra, both being dependent on the modulation amplitude $B_m$. Analyses of these effects have been made by a number of authors based upon the assumption of either a Lorentzian or a Gaussian lineshape (for a review, see [91]). Myers and Putzer [92] derived an expression for the measured signal assuming a Gaussian lineshape, which is typical of the solid materials studied by the CW-NMR system. They began by expressing a generalised Gaussian lineshape in terms of magnetic field units, substituting in equation (13) and expanding it as a Fourier series:

$$
\begin{aligned}
g(B) &= 2T_2\, exp\left[-0.693\left(\frac{B-B_0}{½\Delta B_{½}}\right)^2\right] \\
&= 2T_2\, exp\left[-0.693\left(\frac{B_{ramp}+½B_m \sin\omega_m t}{½\Delta B_{½}}\right)^2\right] \\
&= 2T_2\left[a_0 + \sum_{n=1}^{\infty}\left(a_n \sin n\omega_m t + b_n \cos n\omega_m t\right)\right]
\end{aligned}
\tag{16}
$$

Only the fundamental (first harmonic) component given by the Fourier coefficient $a_1$ is detected in the CW-NMR experiment (since we are employing lock-in detection at the modulation frequency $\omega_m$)

$$
\begin{aligned}
a_1 &= exp\left(-(sB_{ramp})^2\right)\sum_{n=0}^{\infty}\frac{\left(s\,B_m/2\right)^{2n+1}}{2^{2n}}\left(\frac{(2n+1)!}{(n)!(n+1)!}\right) \\
&\times \sum_{k=n+1}^{2n+1}\frac{(-1)^k}{(k)!}\left(\frac{(k)!}{(2k-2n-1)!(2k-2n)!}\right)\left(2\,s\,B_{ramp}\right)^{2k-2n-1}
\end{aligned}
\tag{17}
$$

where $s = 2(ln2)^{½}/\Delta B_{½}$. The effect of the magnetic field modulation on the measured lineshapes is illustrated in the plot of equation (17) in FIG. 7 for several values of $B_m$ normalised to the linewidth $\Delta B_{½}$ [93]. The severe line broadening which results from the use of an excessive $B_m$ is clearly evident. The corresponding maximum signal amplitude as a function of $B_m$ is illustrated in FIG. 8, normalised to the signal amplitude in the absence of field modulation. As $B_m$ increases, the signal increases linearly at first, but levels off and reaches a maximum of $\sim 0.57$ at a field of $B_m/\Delta B_{½} \sim 1.8$, with a steady decrease thereafter. Despite this loss of signal when using field modulation, the large decrease in the measured noise due to the use of narrow bandwidth phase-sensitive detection results in a net improvement in SNR.

## 4.3 Spatial Localisation

If a linear magnetic field gradient $G_x = dB_z/dx$ is superimposed on the main static field $B_0$, the resonant frequency of a nucleus within the sample will depend on its position along the direction of the applied gradient

$$\nu(x) = (\gamma / 2\pi) (B_0 + x \cdot G_x) \tag{18}$$

This is the basis of frequency encoding, which is used exclusively in CW-NMR imaging. The application of such a magnetic field gradient confines the spins that come into resonance to a plane perpendicular to the gradient direction. The effect of the ramped magnetic field $B_{ramp}$ is then to sweep this plane of resonance across the sample in the direction of the gradient. Because magnetic field modulation is employed, the signal from the lock-in amplifier is proportional to the change in the number of spins that are in the plane of resonance. Therefore, the trace over time is the first derivative of the spin density of the sample projected onto the axis of the gradient. Rotating the gradient direction in a fixed plane around the sample results in a series of projections, from which a two-dimensional image can be reconstructed using filtered back-projection. Rotating this plane extends reconstruction of the image to three-dimensions. For 2-D imaging, the gradient direction can be rotated by using a linear combination of two orthogonal gradients $G_x$ and $G_y$ such that

$$G = G_x \sin\theta + G_y \cos\theta \tag{19}$$

where $G$ is the gradient strength. For 3-D imaging, the gradient direction must be rotated in both polar and azimuthal directions to cover four octants in 3-D space. Furthermore, to ensure isotropic resolution, the gradient orientations must be uniformly distributed over the surface of a sphere. Hence, since the elemental area on the surface of a sphere is proportional to $\sin\theta\, d\theta\, d\phi$, as illustrated in FIG. 9, the polar

angle $\theta$ must be stepped uniformly (i.e. $\Delta\theta$ = constant), but the azimuthal angle $\phi$ must be incremented as $1/\sin\theta$, (i.e. $\Delta\phi = \Delta\theta/\sin\theta$). Using the co-ordinate system defined in FIG. 9, the gradient strengths must therefore be varied as

$$\begin{aligned} G_z &= G\sin\vartheta\,\sin\phi \\ G_x &= G\sin\vartheta\,\cos\phi \\ G_y &= G\cos\vartheta \end{aligned} \qquad (20)$$

To cover four octants during 3-D imaging experiments, only the top hemisphere needs to be scanned requiring inversion of the $G_z$ and $G_x$ gradient directions, and hence θ is varied from 0 to 90°, while ϕ is varied from 0 to 360°.

The maximum achievable spatial resolution $(\Delta x)^{-1}$ in CW-NMRI is determined by the natural linewidth $\Delta\nu_{½}$ of the material being studied and by the magnitude of the applied gradient $G$

$$(\Delta x)^{-1} = \gamma G\ (2\pi\Delta\nu_{½})^{-1} \qquad (21)$$

$\Delta\nu_{½}$ can be approximated by $(\pi T_2)^{-1}$ for Lorentzian lineshapes and $(2.13\ T_2)^{-1}$ for Gaussian lineshapes [94]. Therefore, for solid state materials with Gaussian lineshapes, we have

$$(\Delta x)^{-1} \approx 0.34\,\gamma G\,T_2 \qquad (22)$$

Thus, at a gradient strength of 300 mT/m, this corresponds to a maximum theoretical spatial resolution of approximately 0.36 mm for a rigid polymer such as PMMA exhibiting a $T_2$ of 16 μs.

# 5. System Hardware

## 5.1 Overview

A block diagram of the CW-NMRI system is presented in FIG. 10. The system is based around a 7 T, 183 mm diameter horizontal bore superconducting magnet (Oxford Instruments, UK), with a computer (800 MHz PC) controlling certain elements of the system electronics via a GPIB IEEE 488 instrument bus and running the sequence control and data acquisition / processing software. A multifunction data I/O board (National Instruments, USA, Model PCI-MIO-16E-4) was used to enable the input/output of a range of digital and analogue signals to/from the PC for various aspects of experimental control and monitoring. An on-board data buffer together with the in-built timing functionality was used to output all ramp patterns in a precisely time-controlled fashion. A shielded connection block (National Instruments, USA, Model SCB-68) was used as an interface between the I/O board and the equipment rack. The RF was supplied by a synthesiser (Hewlett Packard, USA, Model HP8647A) and applied to one terminal of a hybrid junction (Lorch Electronics, USA, Model JH280E). The two neighbouring ports of the hybrid junction were connected to a 50 Ω load and the resonator, while the signal appearing on the output was sent to a diode detector and low-noise preamplifier unit built in-house, before being passed to the lock-in amplifier (Stanford Research Systems, USA, Model 830 DSP).

All of the software needed to run the CW-NMRI experiment was developed using the LabVIEW programming language (Laboratory Virtual Instrument Engineering Workbench, National Instruments, USA). LabVIEW uses a hierarchical and modular

structure, with higher-level programs (VIs) passing data or parameter lists to lower-lying sub-VIs. Sub-VIs function as stand-alone executables, which aids with the debugging and development of complicated programmes. Furthermore, LabVIEW contains a range of library functions specifically aimed at data acquisition and instrument control, rendering it particularly suitable for the current application. Another useful feature of LabVIEW is the fact that it is a dataflow programming language (by comparison with conventional linear, text-based languages), which means that it can execute multiple operations in parallel, lending greater efficiency to the overall sequence control.

## 5.2 Coil Assembly

The gradient, offset and modulation magnetic fields were produced using a custom-built water-cooled coil assembly (Laplacian Ltd., UK), which employed proprietary stream function designs with power dissipation minimisation to produce large gradient fields (maximum 400 mT/m for the Z and 300 mT/m for the X/Y gradients), together with two nested solenoids producing the ramped offset magnetic field (maximum ± 16 mT) and the superimposed audiofrequency modulation field (maximum ± 400 μT). Overall, the unit had outer and inner diameters of 180 mm and 90 mm respectively. The modulation coil was placed on the inside layer of the assembly to minimise its inductance and hence current requirements, while the offset coil was placed on the outside to minimise its coupling to the modulation coil. All magnetic fields were homogeneous to within 5 % over a cylindrical volume of diameter 50 mm and length 70 mm. Commercial power supplies (Advance Hivolt, UK, Models AP90100 and AP5060) were used to power the gradient and offset coils (with maximum current capabilities of 90 A and 50 A respectively), while a home-

built audiofrequency power supply was used to drive the modulation coil up to a maximum frequency of 15 kHz. Temperature sensors were placed at various hotspots within the assembly and continually monitored during experiments. The physical characteristics of the coil assembly are listed in Table 1.

## 5.3 Resonators

All of the resonators used with the CW-NMRI system were based on an 8- or 12-leg birdcage design described previously [88]. In each case, it was necessary to avoid using materials in the construction of the resonators which contained the nuclei of interest, since these would be detected by the system and hence contribute a significant background signal. Thus, PTFE was typically used to provide structural support, while specialised non-magnetic capacitors were used throughout (fixed capacitances formed using miniature chip ceramic capacitors (Tekelec, France) or appropriately-shaped strips of CuFlon (Polyflon, USA), which is comprised of copper electroplated onto both sides of a thin dielectric of PTFE; and Voltronics variable capacitors (Voltronics, USA)). The resonators were placed directly into RF shields made from copper sheets of thickness 0.5 mm and length 200 mm, with a resultant outer diameter of 81 mm. It was necessary to split the shields along their length to prevent the audiofrequency magnetic field modulation causing eddy currents, which would introduce acoustic interference and would also prevent the modulation from penetrating the shield to the sample. This split was typically closed to RF penetration by forming a capacitor comprising the shield itself and a strip of copper (width 18-80 mm, thickness 40-80 μm depending on the resonant frequency) bridging the gap, with a strip of PTFE (thickness 55 μm) in between acting as a dielectric.

## 5.4 Automatic Frequency Controller (AFC)

In a CW-NMRI experiment, it is essential to ensure that the resonator is maintained exactly on-tune in order to eliminate the dispersive component of the RF susceptibility and thus only detect the absorption component. However, factors such as thermal expansion, sample loading and microphonics can lead to drifting of the resonator's frequency, and therefore it is vital to be able to track such frequency drifts. In practice, this was achieved by dynamically controlling the frequency transmitted by the RF synthesiser using a home-built automatic frequency controller (AFC) [95] so as to equalise the transmitted frequency and the resonator's central frequency. This was implemented using a feedback loop from the output of the hybrid junction to the RF synthesiser (FIG. 10). By effectively operating at a different frequency in this manner, the static field $B_0$ needs to be adjusted to maintain the resonance condition, i.e. $\omega_0$ is effectively changed to follow drifting of the resonator during the course of an experiment. This adjustment of the static field $B_0$ was done by adding a dc offset shift to the ramped magnetic field when sweeping through the resonant peak.

The AFC controls the operating frequency by imposing a frequency modulation at 33 kHz onto the signal transmitted by the RF synthesiser (300 MHz for $^1$H work). At resonance, the 33 kHz frequency modulation (FM) is converted to a 66 kHz amplitude modulation (AM) of the reflected signal (see FIG. 11(c)). If the resonator drifts away from resonance, the signal from the hybrid junction will contain AM components at both 33 kHz and 66 kHz (FIG. 11(a), (b) and (c)). The amplitude of the 33 kHz component increases as the resonator drifts further from resonance, while its phase is sensitive to the direction of the drift. Part of this reflected signal is then fed back into

the AFC, where it inputs to a phase sensitive detector (PSD). The PSD compares this signal with a reference signal deriving from the source of the original 33 kHz modulation, and outputs a dc error signal proportional to the frequency drift of the resonator. This dc error signal is added to the 33 kHz modulation signal, and applied to the 'DC FM' input of the RF synthesiser. The RF synthesiser's transmitted frequency can be varied by ± 50 kHz with the application of a ± 1 V dc error signal, which corresponds to a magnetic field of ± 1.16 mT at 300 MHz.

## 5.5 Detector

Before describing the operation of the detector circuit, it is instructive to summarise the various signals along different pathways in the CW-NMRI system. These are illustrated in FIG. 12.

The 15 V dc signal added to the output of the AFC is stripped from the other components using the capacitor C and is used to power the detector and preamplifier circuitry. Meanwhile, the 300 MHz and 33 kHz components pass onto the hybrid junction without attenuation because of the greater impedance presented by the resistor R compared to the capacitor. The output from the hybrid junction to the detector contains the 300 MHz and 33 kHz components, together with the absorption signal at 881 Hz (variable up to 15 kHz). The detector strips off the 300 MHz component and outputs the 33 kHz component, the 881 Hz absorption signal, plus a "dc bias" voltage which indicates the actual operating bias voltage of the diode detector. These signals arrive at the AFC, which removes the dc component (which can be monitored at the AFC) before forwarding the 881 Hz and 33 kHz components

to the lock-in amplifier. The PSDs in the lock-in amplifier and AFC are only sensitive to the 881 Hz and 33 kHz components respectively, and disregard the rest.

The main elements in the diode detector are illustrated in FIG. 13. A diode detector essentially takes an RF signal, rectifies it, filters it to remove the high frequency component, and outputs a dc signal proportional to the RF input level. The detector built for the CW-NMRI system uses a pair of Schottky diodes $S_1$ and $S_2$ in bi-phase arrangement, which doubles the output signal compared to using just one diode since both half cycles of the RF waveform are detected. Resistors $R_1$ and $R_2$ set the required bias for the diodes. Capacitor $C_1$ couples the incoming signal to the circuit, while $C_2$ forms an RC circuit (with $R_1$) with a time constant of ~ 32 ns, which effectively smoothes the rectified RF signal to a dc level proportional to the input RF power. The 33 kHz and 881 Hz signals superimposed on the 300 MHz carrier wave are not rectified, nor do they 'see' this RC circuit because of its short time constant and so pass through it unaffected. Thus the signal arriving at point *A* consists of the 33 kHz and 881 Hz components with a superimposed dc component. This dc component is prevented from entering the pre-amplifier circuit by $C_3$, and instead follows the path directly to the output. The 33 kHz and 881 Hz signals are prevented from following the dc component because of the large impedance presented to them by $R_3$, and therefore pass into the pre-amplifier. The amplified components are finally added to the dc bias voltage at the output. The detector and pre-amplifier circuit was encased in a die-cast alloy box which was placed as close as possible to the resonator.

## 5.6 Support Frame

The resonator/shields were mechanically decoupled from the main gradient, ramp and modulation coil assembly by sliding them into a 1.6 m-long fibreglass tube (1 mm wall thickness, inner diameter 83 mm) which was suspended within the coil assembly using two support frames built at either end of the magnet (FIG. 14 (a)). The frames did not touch either the coil assembly or the magnet at any point and furthermore were mounted on vibration-dampening feet, in an effort to minimise microphonic effects due to vibrations originating in the modulation coil. A system for suspending and accurately positioning samples within the magnet was also incorporated into the support frame. Sample holders were typically made from PTFE to avoid background signal pick-up and attached to a three-way translational stage on the positioning platform via a quartz rod (FIG. 14 (b)).

# 6. Applications

## 6.1 Imaging of Cementitious Materials

The deterioration over time of reinforced concrete structures is of major economic significance throughout the world. The presence of water and water transport is known to play a key role in determining the pore structure and long-term durability of cement materials, which constitute the key component of concretes. For example, an excess of water during fabrication leads to large pore sizes and hence a high permeability in the material. This results in enhanced water ingress, which causes problems on a number of fronts: direct physical attack via freeze-thaw mechanisms; chemical leaching of the calcium hydroxide phase in the cement by the hydration of calcium silicates; direct damage caused by salt crystallisation; effects of various

dissolved ion species, for example dissolved sulphate ions directly attacking calcium aluminate phases, and dissolved chloride ions corroding the steel in reinforced structures [96]. Bridges and coastal structures are particularly exposed to the ingress of salty water, while de-icing on motorways via salt gritting can also cause significant problems. However, the movement of dissolved ions such as sodium and chloride within cements is still not fully understood, while the reactions which may take place between them and the cement material itself or additives within the cement are equally vague. It is therefore of considerable interest to characterise water content and transport in cement materials in a spatially resolved, non-invasive and non-destructive manner which will allow time-course studies to be carried out.

The CW-NMRI system was used to study the penetration of water and brine into samples fabricated from Ordinary Portland Cement (OPC), using various water/cement (w/c) ratios and curing conditions to produce a range of samples with differing pore size distributions. In general, one-dimensional profiling experiments were carried out on cylindrically-shaped samples measuring up to 44 mm in diameter and 60 mm in length, with a typical acquisition time of 4 minutes per profile.

### *6.1.1 Water Penetration*

A sample with a water/cement ratio of 0.4 by weight (which is at the threshold water content required for complete hydration of OPC) was cured for 28 days in a dry desiccator with a relative humidity of < 5 %. All surfaces of the sample except the top face were sealed with Parafilm, to promote evaporation of water through this surface only. This was done to disrupt the hydration process in this part of the sample and hence introduce some inhomogeneity into the cured sample. Following the cure

period, the Parafilm was removed and the sample was dried in an oven for 48 hours at 105°C in order to remove all evaporable water. Water penetration studies were then carried out as described below.

One-dimensional profiling experiments carried out on the sample during curing and drying are illustrated in FIG. 15. It can be seen that there is a gradual decrease in intensity on the left-hand side of the profile, consistent with a loss of water from this part of the sample through evaporation from the exposed face. It should be noted that the CW-NMRI technique detects water protons in all environments within the sample, that is capillary water, gel water *and* chemically-combined water. Consequently, any decrease in the measured intensity results from a loss of water from the sample, rather than a loss of signal due to an increasing proportion of chemically-combined water as the hydration progresses. The maximum non-uniformity measured along the sample occurred after 14 days of curing, after which the profile began to level off as water diffused from the right side of the sample and was eventually lost through evaporation. There was no further decrease in intensity or indeed sample mass after 24 hours of drying, and hence the 24-hour profile is a measure of the chemically-combined water content within the sample. Note the residual slope to the left hand side in this profile, indicating an inhomogeneous cure along the axis of the sample. At this point, the sample exhibited a $T_2^*$ of ~ 10 μs.

FIG. 16 shows the penetration of water into the cured and dried sample. The sample's orientation was as before, with the exposed face to the left side. The water reservoir was on the right side and was removed while profiling. A water front can be seen moving across the sample, reaching the left side after approximately 6 hours of

soaking. Thereafter, the intensity of the profile increased over a period of tens of hours, consistent with the gradual filling of smaller pores within the sample. Two effects can be discerned. Firstly, the intensity peaks after 24 hours of soaking, but exhibits a fall-off to the right, indicating enhanced uptake of water in the left part of the sample. This is consistent with an incomplete hydration in this region of the sample due to water evaporation during the curing process, which would result in a more porous structure and hence an enhanced uptake of water. Secondly, the intensity of the profile decreased following further soaking, reaching a steady state after about 90 days (see insert in FIG. 16). This situation represents a dynamic equilibrium in the sample between uptake of water from the reservoir on the right and loss of water via evaporation from the left face.

The sample was dried completely and a second water penetration experiment was carried out. The maximum uptake of water occurred once again after 24 hours of soaking; however, the slope of the profile was less pronounced, as illustrated in FIG. 17. Furthermore, the peak intensity was lower in the second experiment, which is evidence of a smaller pore size distribution in the sample, suggesting that some degree of rehydration took place in this sample during the course of the first water penetration study. This result was further verified by mercury intrusion porosimetry.

2-D imaging of water penetration into a sample of OPC is illustrated in FIG. 18. This sample, measuring 32 x 30 x 12 mm, was cured for 28 days in a wet environment (relative humidity > 95 %) to ensure a homogeneous cure, and dried at 105°C for 48 hours to remove all evaporable water. The sample was then completely sealed except for the left face, which was exposed to a water reservoir. The water reservoir

was removed for imaging, and an acquisition time of 15 minutes was used for each image (there was negligible penetration of the absorbed water into the sample while the water reservoir was removed). It can be seen in FIG. 18 that the water has almost fully penetrated across the sample after approximately 1 hour of soaking, with a further increase in intensity after prolonged soaking, again consistent with the filling of smaller pores within the sample. Note that the signal in the right part of FIG. 18(a) derives solely from the chemically combined water in the sample, with a $T_2^*$ of approximately 10 μs. The imbibed water exhibited a $T_2^*$ of approximately 30 μs.

### *6.1.2 Brine Penetration*

The penetration of brine into a range of OPC samples (with w/c ratios of 0.3, 0.4 and 0.5) was studied. The samples were cured for 28 days in a wet environment (relative humidity > 95 %) to ensure a homogeneous cure, and dried at 105°C for 48 hours to remove all evaporable water. After drying, the samples were immediately placed into a saturated solution of NaCl for 4 days, after which the samples were fully saturated. The samples were then removed from the solution and imaged. The resulting 1-D profiles are presented in FIG. 19, where an increase in the signal is observed as the w/c ratio is increased, due to the increased pore sizes and hence increased uptake.

In a second set of experiments, the rate of penetration of a brine solution into a cement sample was measured as a function of soaking time. The sample, which had a w/c ratio of 0.4, was heated in an oven at 105°C for 4 days to remove all evaporable water, and then sealed on all sides except the end face which was dipped in a saturated salt solution. The resulting 1-D profiles illustrated in FIG. 20 show the progression of the $^{23}Na$ front into the sample with prolonged soaking times.

### *6.1.3 Imaging of Solid $^{27}Al$ in Cement*

In addition to their binding properties, modern cements are characterised by a range of physical properties such as their rate of hardening, their resistance to ageing and temperature extremes, their rheological properties, and their interaction with the fillers and additives typically used in the mix. These properties are determined by the mineralogical composition of the cement, which are generally tailored to suit the particular application. For example, for high temperature refractory applications, cements with high content of $Al_2O_3$ have been developed which afford the cement a very quick setting time and extremely high temperature resistance. Understanding the extent of the hydration reaction of the various components within these materials can aid in determining their long-term durability, and hence the ability to image the various phases in the cement is highly desirable.

A series of samples with water/cement ratios of 0.3, 0.4 and 0.5 were made using a high temperature refractory cement called Secar 80® (Lafarge Aluminates, France). This calcium aluminate cement consists of approximately 80 % $Al_2O_3$ and 17 % CaO, together with trace amounts of other elements (for comparison, OPC contains only ~ 12 % $Ca_3Al_2O_6$ and ~ 8 % $Ca_4Al_2Fe_2O_{10}$). The samples, measuring 44 mm in diameter and 60 mm in length, were cast in cylindrical moulds and cured for 28 days in an environment with a relative humidity of > 95 %. Spectroscopic evaluation of the $^{27}Al$-containing phase of the fully-cured samples indicated a $T_2$ relaxation time of 49 ± 1 μs. The 1-D profiles presented in FIG. 21 are of the $^{27}Al$ chemically combined within the $Al_2O_3$ phase in the cement. The decrease in the measured $^{27}Al$ signal of these samples as the w/c ratio is increased is clearly evident, demonstrating

that the CW-NMRI system is sensitive to differences in the local cement concentration. It is interesting to note the slope to the right side (which corresponds to the top of the samples) for the w/c = 0.4 and 0.5 samples, which indicates that some degree of sedimentation may have taken place during the early stages of the cure.

A section of dimension 60 x 34 x 32 mm was cut from the w/c = 0.3 sample. Two holes with diameters 6 mm and 8 mm were drilled through the sample, and a 2-D image (FIG. 22 (a)) was acquired using an acquisition time of 16 hours. The image was deconvolved with the sample's zero gradient spectrum using a modified Weiner filter algorithm, resulting in an improvement in spatial resolution (FIG. 22 (b)).

## 6.2 Diffusion of Water in Clay Minerals

The three-layered clay mineral montmorillonite (bentonite) is characterised by a low hydraulic conductivity and a capacity to bind water molecules and positively charged ions (cations). As such, water-saturated compacted bentonite powder is used as a hydrological barrier in areas such as waste disposal, for example around land-fill sites where the desire is to prevent leakage of contaminants from the land-fill into the surrounding environment. It is also used in underground nuclear waste repositories as a barrier to radionuclide diffusion, where a layer of water-saturated, compacted bentonite is coated on the outside of a steel canister containing the radioactive waste. Here, the interest is in preventing ground-water from penetrating through to the canister, where dissolved elements may corrode the steel, but also in preventing dissolved radionuclides from leaking out in the event of a compromised canister. The excellent sorption capacity of bentonite for cationic radionuclides is key in this regard. However, bentonite is generally ineffective in adsorbing anionic contaminants such as

the long-lived $^{129}I$ and $^{99}Tc$. The migration of such contaminants is expected to be dominated by diffusion processes, and thus it is of considerable interest to measure the diffusion coefficient of water in compacted bentonite.

Conventional MRI has been successfully used to measure diffusion coefficients in a broad range of materials using field-gradient diffusometry techniques. However, such an approach is not possible for samples of bentonite due to the extremely short transverse relaxation times which this material exhibits, particularly for samples with relatively low water contents in the region of 20 to 30 %, which is the water content typically used in the environmental technology applications mentioned above. An alternative approach to diffusometry via NMR employed in the present work is the observation of the temporal evolution of 1-D substance profiles by CW-NMRI, which can be used to determine the diffusion coefficient of the substance of interest. However, in contrast to field-gradient NMR, this approach cannot be used to observe pure self-diffusion, but rather one is constrained to study either diffusion processes along a moisture gradient (inter-diffusion) or the propagation of a stable isotope tracer profile (i.e. the diffusive mixing between ordinary water and deuterium oxide in the case of water self-diffusion in clay).

Clay samples were prepared in PTFE containers with an inner diameter of 30 mm and a length of 50 mm. Laboratory grade bentonite powder was obtained from Sigma-Aldrich (Poole, UK) and mixed in powder form with the appropriate quantities of water or heavy water ($D_2O$). After mixing, the moistened powder was filled in several layers into the sample container. Each layer was condensed into a homogeneous clay mass by heavily stamping with a rounded metal bar for several

minutes. To create an interdiffusion scenario along a moisture gradient, a sample consisting of a homogeneous bentonite layer with a water content of 20 wt% was brought into contact with a reservoir of laboratory tissue paper soaked with several ml of deionised water. In a separate experiment, the self-diffusion of water between two bentonite layers prepared with light and heavy water was studied. The water content in this case was chosen to be 30 wt% for the light water and 33.3 wt% for the heavy water.

The results of these experiments are presented in FIG. 23. The profiles in FIG. 23(a) show the concentration-driven diffusion water front moving into the bentonite sample. The right side of the sample was confined at the bottom of the sample container, and hence swelling of the sample as it progressively absorbed more water is evident at the interface between the bentonite and tissue. In FIG. 23(b), some residual $H_2O$ content is evident on the left side of the sample despite heating the bentonite powder at 70°C for 3 days in an attempt to remove all evaporable water. The absorption of atmospheric water by the highly hygroscopic bentonite powder and pick-up from $^1H$ in OH groups within the alumina layers of the bentonite account for this signal. Nevertheless, the gradual diffusion of the $H_2O$ through the sample is clear.

In both cases, an analysis of the diffusion front as a function of time shows a $t^2$-dependence of the front line which indicates Fickian diffusion and allows for the determination of a diffusion coefficient according to $x^2 = 2Dt$ from the slope of the curves in FIG. 24. The interdiffusion coefficient was measured at $[1.15 \pm 0.05] \times 10^{-9}$ m$^2$/s, while the self-diffusion coefficient was measured at $[8.4 \pm 0.5] \times 10^{-10}$ m$^2$/s, which is the same order of magnitude as that recorded for

non-swelling technical-grade kaolinite at similar water content [97]. This indicates that the difference in molecular dynamics between bentonite and kaolinite clays (which is quite obvious from the different NMR relaxation behaviour of both materials) does not lead to a strong effect on the long-range diffusive transport behaviour of the water molecules and that the tortuosities encountered by the molecules are similar.

## 6.3 Imaging of a Rigid Polymer

The imaging performance of the CW-NMRI system can be demonstrated by showing 2- and 3-D images of a rigid polymer such as poly(methyl methacrylate) (PMMA) (Perspex / Plexiglas). Spectroscopic investigations carried out on this material indicated the presence of both crystalline and semi-amorphous phases (relative proportions 80:20), with $T_2^*$ values of 16.3 μs and 26.9 μs respectively. The maximum achievable spatial resolution for this material is illustrated by reference to FIG. 25. The resolution phantom, shown schematically in FIG. 25(a), was imaged using a gradient strength of 300 mT/m and an acquisition time of 1.8 hours. The 1 mm hole is just resolved in the raw image of FIG. 25(b), while the 0.75 mm hole is resolved in the deconvolved image in FIG. 25(c). A 3-D phantom, shown schematically in FIG. 26(a), was imaged using a gradient strength of 300 mT/m. In total, 5102 one-dimensional line projections were acquired at different angles around the sample, resulting in an acquisition time of 8.5 hours. 3-D surface rendered views of the phantom are presented in FIG. 26(b) and (c).

# 7. Concluding Remarks

The work carried out in this research has shown that CW-NMRI is a valuable addition to the armoury of techniques available for the non-invasive imaging of solid materials by magnetic resonance. Although there exists scope for further improvements to the system, most notably in reducing imaging time (several strategies are currently being considered), the advantages inherent to the continuous wave approach to NMR imaging have already rendered amenable to study a broad range of materials, and should lead to CW-NMRI becoming a standard technique in this field.

# Acknowledgements

The authors would like to thank Dr. Gareth Davies and Prof. Jim Hutchison for help with various aspects of experimental design and construction, Prof. Fredrik Glasser for help and advice with the cement studies, Dr. Nikolaus Nestle (TU, Darmstadt) for collaboration with the bentonite work, and Dr. Yuanmu Deng (Ohio State University) for help with the reconstruction of the 3D dataset. We are also indebted to Mr. Eddie Stevenson and Mr. Peter Frew for workshop assistance. This work was funded by the UK Engineering and Physical Sciences Research Council (Grant Number GR/R02269/01).

# References


1. P. Blumler and B. Blumich, Springer, Berlin, 1994, **30**, 208.
2. P. Jezzard, J. J. Attard, T. A. Carpenter, and L. D. Hall, *Prog. Nuc. Mag. Res. Sp.*, 1991, **23**, 1.
3. D. E. Demco and B. Blumich, *Concept Magnetic Res.*, 2000, **12**, 188.
4. E. R. Andrew and E. Szczesniak, *Prog. Nuc. Mag. Res. Sp.*, 1995, **28**, 11.
5. G. C. Chingas, J. B. Miller, and A. N. Garroway, *J. Magn. Reson.*, 1986, **66**, 530.
6. D. G. Cory, J. B. Miller, R. Turner, and A. N. Garroway, *Mol. Phys.*, 1990, **70**, 331.
7. D. G. Cory, *Solid State Nucl. Mag.*, 1996, **6**, 347.
8. K. Takegoshi and C. A. McDowell, *Chem. Phys. Lett.*, 1985, **116**, 100.
9. S. Matsui, *Chem. Phys. Lett.*, 1991, **179**, 187.
10. S. Hafner, D. E. Demco, and R. Kimmich, *Solid State Nucl. Mag.*, 1996, **6**, 275.
11. D. G. Cory, J. W. M. van Os, and W. S. Veeman, *J. Magn. Reson.*, 1988, **76**, 543.
12. S. Hafner and H. W. Spiess, *Concept Magnetic Res.*, 1998, **10**, 99.
13. F. De Luca and B. Maraviglia, *J. Magn. Reson.*, 1986, **67**, 169.
14. A. A. Samoilenko, D. Y. Artemov, and L. A. Sibeldina, *JETP Lett+*, 1988, **47**, 417.
15. P. J. McDonald and B. Newling, *Rep. Prog. Phys.*, 1998, **61**, 1441.
16. S. P. Cottrell, M. R. Halse, and J. H. Strange, *Meas. Sci. Techol.*, 1990, **1**, 624.
17. A. N. Garroway, J. Baum, M. G. Munowitz, and A. Pines, *J. Magn. Reson.*, 1984, **60**, 337.
18. B. H. Suits and D. White, *Solid State Commun.*, 1984, **50**, 291.
19. H. S. Gutowsky, G. B. Kistiakowsky, and E. M. Purcell, *J. Chem. Phys.*, 1949, **17**, 972.
20. E. von Meerwall, R. B. Creel, C. F. Griffin, E. DiCato, F. T. Lin, and F. M. Lin, *J. Appl. Polym. Sci.*, 1977, **21**, 1489.
21. J. Pacanovsky, F. N. Kelley, and E. von Meerwall, *J. Polym Sci Pol. Phys.*, 1994, **32**, 1339.
22. P. C. Lauterbur, C. S. Dulcey Jr., C. M. Lai, M. A. Feiler, W. V. House Jr., D. Kramer, C.-N. Chien, and R. Dias, 1974, **1**, 27.
23. D. J. Lurie, S. J. McCallum, J. M. S. Hutchison, and M. Alecci, *MAGMA*, 1996, **4**, 77.
24. S. D. Beyea, B. J. Balcom, I. V. Mastikhin, T. W. Bremner, R. L. Armstrong, and P. E. Grattan-Bellew, *J. Magn. Reson.*, 2000, **144**, 255.
25. F. De Luca, N. Lugeri, S. Motta, G. Cammisa, and B. Maraviglia, *J. Magn. Reson. A*, 1995, **115**, 1.
26. M. Klinkenberg, P. Blumler, and B. Blumich, *J. Magn. Reson. A*, 1996, **119**, 197.
27. P. Barth, S. Hafner, and W. Kuhn, *J. Magn. Reson. A*, 1994, **110**, 198.
28. P. M. Glover, P. J. McDonald, and B. Newling, *J. Magn. Reson.*, 1997, **126**, 207.

29. D. E. Axelson, A. Kantzas, and A. Nauerth, *Solid State Nucl. Mag.*, 1996, **6**, 309.
30. M. R. Halse, H. J. Rahman, and J. H. Strange, *Physica B*, 1994, **203**, 169.
31. M. Bogdan, B. J. Balcom, T. W. Bremner, and R. L. Armstrong, *J. Magn. Reson. A*, 1995, **116**, 266.
32. T. Nunes, E. W. Randall, A. A. Samoilenko, P. Bodart, and G. Feio, *J. Phys. D: Appl. Phys.*, 1996, **29**, 805.
33. B. J. Balcom, in *Spatially Resolved Magnetic Resonance*, Wiley-VCH, Weinheim, Germany, 1998, p. 75.
34. M. A. Baumann, G. M. Doll, and K. Zick, *Oral. Surg. Oral. Med. O.*, 1993, **75**, 517.
35. C. H. Lloyd, S. N. Scrimgeour, G. Hunter, J. A. Chudek, D. M. Lane, and P. J. McDonald, *J. Mater. Sci. -Mater. M.*, 1999, **10**, 369.
36. A. Abragam, *The Principles of Nuclear Magnetism*, Oxford University Press, New York, 1961
37. P. T. Callaghan, *Principles of Nuclear Magnetic Resonance Microscopy*, Clarendon Press, Oxford, 1991
38. P. J. McDonald, *Prog. Nuc. Mag. Res. Sp.*, 1997, **30**, 69.
39. D. E. Demco and B. Blumich, *Concept Magnetic Res.*, 2000, **12**, 269.
40. B. Blumich, *NMR Imaging of Materials,* Clarendon Press, Oxford, 2000
41. M. J. D. Mallett, M. R. Halse, and J. H. Strange, *J. Magn. Reson.*, 1998, **132**, 172.
42. J. Godward, E. Ciampi, M. Cifelli, and P. J. McDonald, *J. Magn. Reson.*, 2002, **155**, 92.
43. G. Eidmann, R. Savelsberg, P. Blumler, and B. Blumich, *J. Magn. Reson. A*, 1996, **122**, 104.
44. B. Blumich, P. Blumler, G. Eidmann, A. Guthausen, R. Haken, U. Schmitz, K. Saito, and G. Zimmer, *Magn. Reson. Imaging*, 1998, **16**, 479.
45. P. M. Glover, P. S. Aptaker, J. R. Bowler, E. Ciampi, and P. J. McDonald, *J. Magn. Reson.*, 1999, **139**, 90.
46. Y. M. Daud and M. R. Halse, *Physica B*, 1992, **176**, 167.
47. M. J. D. Mallett, S. L. Codd, M. R. Halse, T. A. P. Green, and J. H. Strange, *J. Magn. Reson. A*, 1996, **119**, 105.
48. J. H. Strange, *Philos. T. Roy. Soc. A*, 1990, **333**, 427.
49. S. L. Codd, M. J. D. Mallett, M. R. Halse, J. H. Strange, W. Vennart, and T. van Doom, *J. Magn. Reson. B*, 1996, **113**, 214.
50. J. B. Miller and A. N. Garroway, *J. Magn. Reson.*, 1989, **82**, 529.
51. S. Emid, *Physica B & C*, 1985, **128**, 79.
52. Z. H. Cho and Y. M. Ro, *Magn. Reson. Med.*, 1994, **32**, 258.
53. M. A. Fernandez-Seara, S. L. Wehrli, and F. W. Wehrli, *J. Magn. Reson.*, 2003, **160**, 144.
54. B. J. Balcom, R. P. MacGregor, S. D. Beyea, D. P. Green, R. L. Armstrong, and T. W. Bremner, *J. Magn. Reson. A*, 1996, **123**, 131.
55. S. D. Beyea, B. J. Balcom, P. J. Prado, A. R. Cross, C. B. Kennedy, R. L. Armstrong, and T. W. Bremner, *J. Magn. Reson.*, 1998, **135**, 156.
56. P. J. Prado, B. J. Balcom, S. D. Beyea, R. L. Armstrong, and T. W. Bremner, *Solid State Nucl. Mag.*, 1997, **10**, 1.
57. P. Szomolanyi, D. Goodyear, B. Balcom, and D. Matheson, *Magn. Reson. Imaging*, 2001, **19**, 423.

58. M. R. Halse, D. J. Goodyear, M. MacMillan, P. Szomolanyi, D. Matheson, and B. J. Balcom, *J. Magn. Reson.*, 2003, **165**, 219.
59. R. R. Ernst, G. Bodenhausen, and A. Wokaun, *Principles of Nuclear Magnetic Resonance in One and Two Dimensions,* Clarendon Press, Oxford, 1987
60. G. Bodenhausen, *Prog. Nuc. Mag. Res. Sp.*, 1980, **14**, 137.
61. E. Gunther, B. Blumich, and H. W. Spiess, *Mol. Phys.*, 1990, **71**, 477.
62. H. Geen, R. Graf, A. S. D. Heindrichs, B. S. Hickman, I. Schnell, H. W. Spiess, and J. J. Titman, *J. Magn. Reson.*, 1999, **138**, 167.
63. A. Jerschow, J. W. Logan, and A. Pines, *J. Magn. Reson.*, 2001, **149**, 268.
64. C. Filip, X. Filip, M. Bertmer, D. E. Demco, and B. Blumich, *J. Magn. Reson.*, 2001, **150**, 184.
65. T. Karlsson, M. Eden, H. Luthman, and M. H. Levitt, *J. Magn. Reson.*, 2000, **145**, 95.
66. A. Wiesmath, C. Filip, D. E. Demco, and B. Blumich, *J. Magn. Reson.*, 2001, **149**, 258.
67. E. R. Andrew, A. Bradbury, and R. G. Eades, *Nature*, 1959, **183**, 1802.
68. I. J. Lowe, *Phys. Rev. Lett.*, 1959, **2**, 285.
69. E. Gunther, B. Blumich, and H. W. Spiess, *Chem. Phys. Lett.*, 1991, **184**, 251.
70. U. Scheler, G. Schauss, B. Blumich, and H. W. Spiess, *Solid State Nucl. Mag.*, 1996, **6**, 375.
71. M. Lee and W. I. Goldberg, *Phys. Rev.*, 1965, **140**, A1261.
72. A. E. Medfed and V. A. Atsarkin, *JETP Lett+*, 1977, **25**, 215.
73. F. De Luca, A. Gargaro, B. Maraviglia, G. H. Raza, and C. Casieri, *Magn. Reson. Imaging*, 1998, **16**, 435.
74. F. De Luca, E. De Vita, G. H. Raza, and C. Casieri, *J. Magn. Reson.*, 1999, **139**, 126.
75. E. D. Ostroff and J. S. Waugh, *Phys. Rev. Lett.*, 1966, **16**, 1097.
76. P. Mansfield and D. Ware, *Phys. Lett.*, 1966, **22**, 133.
77. J. S. Waugh, L. M. Huber, and U. Haeberlen, *Phys. Rev. Lett.*, 1968, **20**, 180.
78. P. Mansfield, *J. Phys. C: Solid State*, 1971, **4**, 1444.
79. D. P. Burum and W. K. Rhim, *J. Chem. Phys.*, 1979, **71**, 944.
80. P. Mansfield and P. K. Grannell, *Phys. Rev. B*, 1975, **12**, 3618.
81. D. G. Cory, in *Magnetic Resonance Microscopy,* VCH, Weinheim, Germany, 1992, p. 49.
82. J. B. Miller, D. G. Cory, L. G. Butler, and A. N. Garroway, *Magn. Reson. Imaging*, 1992, **10**, 789.
83. D. G. Cory, A. M. Reichwein, J. W. M. van Os, and W. S. Veeman, *Chem. Phys. Lett.*, 1988, **143**, 467.
84. Y. H. Sun, J. C. Xiong, H. Lock, M. L. Buszko, J. A. Haase, and G. E. Maciel, *J. Magn. Reson. A*, 1994, **110**, 1.
85. M. Buszko and G. E. Maciel, *J. Magn. Reson. A*, 1994, **110**, 7.
86. W. K. Rhim, A. Pines, and J. S. Waugh, *Phys. Rev. B*, 1971, **3**, 684.
87. S. Hafner, P. Barth, and W. Kuhn, *J. Magn. Reson. A*, 1994, **108**, 21.
88. G. R. Davies, D. J. Lurie, J. M. S. Hutchison, S. J. McCallum, and I. Nicholson, *J. Magn. Reson.*, 2001, **148**, 289.
89. A. J. Fagan, G. R. Davies, J. M. S. Hutchison, and D. J. Lurie, *J. Magn. Reson.*, 2003, **163**, 318.
90. A. J. Fagan, N. Nestle, and D. J. Lurie, *Magn. Reson. Imaging*, in print.
91. C. P. Poole, *Electron Spin Resonance: A Comprehensive Treatise on Experimental Techniques, 2nd Ed.* Wiley-Interscience, New York, 1983

92. O. E. Myers and E. J. Putzer, *J. Appl. Phys.*, 1959, **30**, 1987.
93. S. J. McCallum, Ph.D. Thesis, University of Aberdeen, 1998
94. C. P. Poole and H. A. Farach, *Relaxation in Magnetic Resonance,* Academic Press, London, 1971
95. M. Alecci, S. J. McCallum, and D. J. Lurie, *J. Magn. Reson. A*, 1995, **117**, 272.
96. A. Chowdhury, A. Gillies, P. J. McDonald, and M. Mulheron, *Mag. Concrete Res.*, 2001, **53**, 347.
97. N. Nestle, in *Integrated Environmental Technology Series*, IWA Publishing, London, 2005, in press.
98. A. J. Fagan, G. R. Davies, J. M. S. Hutchison, F. P. Glasser, and D. J. Lurie, *J. Magn. Reson.*, in print.
99. R. Turner, *Magn. Reson. Imaging*, 1993, **11**, 903.

## Figure Legends

FIG. 1. Geometry of the magnetic dipole-dipole interaction. $\theta_{ij}$ and $\Phi_{ij}$ are the polar and azimuthal angles respectively of the internuclear vector $r_{ij}$.

FIG. 2. A typical timing diagram used with the oscillating gradient technique to produce gradient echoes (Adapted from [16])

FIG. 3. (a) The original magic sandwich echo (MSE) sequence (Adapted from [86]); (b) 180° pulses replaced by continuous RF irradiation (Adapted from [8]).

FIG. 4. Block diagram of the CW-NMR spectrometer.

FIG. 5. The signal (horizontal) produced at various points on the resonant line due to the magnetic field modulation (vertical) (adapted from [91]).

FIG. 6. (a) Signal arriving at the detector (a) with no field modulation and (b) with field modulation (adapted from [91]).

FIG. 7. Effect of magnetic field modulation on the measured lineshape according to equation (17).

FIG. 8. Variation in the signal amplitude with $B_m$, normalised to the signal amplitude in the absence of field modulation according to equation (17).

FIG. 9. Co-ordinate system for 3-D imaging sequence, illustrating the acquisition scheme for isotropic resolution.

FIG. 10. Block diagram of the principal components in the CW-NMRI system.

FIG. 11. Response to the 33 kHz modulation of the AFC: (a) far off resonance, (b) on resonance and (c) and (d) close to and either side of resonance (adapted from [91]).

FIG. 12. Block diagram showing the various signals along different pathways in the CW-NMRI system (for $^1H$ work).

FIG. 13. Schematic diagram of the diode detector circuit.

FIG. 14. (a) Photograph of the frame supporting the shield/resonator and sample holder, and (b) close-up of the 3-way translational stage for accurate positioning of the sample.

FIG. 15. Profiles of an inhomogeneously cured w/c = 0.4 sample for different curing and drying times. A gradient of 140 mT/m was used. The unsealed face was on the left side. The peak to the left of the sample is from a reference material.

FIG. 16. Water penetration into a w/c = 0.4 sample as a function of soaking time, reaching a peak after 24 hours of soaking – the water reservoir was on the right side. The insert shows the decrease in intensity after 7 and 9 days of soaking, indicating the establishment of a dynamic equilibrium within the sample between water absorption from the reservoir on the right and evaporation on the left.

FIG. 17. Comparison of the peak water uptake into the w/c = 0.4 sample during the first and second water penetration experiments.

FIG. 18. Water penetration into a cement sample following soaking times of: (a) 5 minutes, (b) 10 minutes, (c) 15 minutes, (d) 30 minutes, (e) 60 minutes and (f) 5 hours. Image acquisition times = 15 minutes (reproduced from [89] with permission from Elsevier).

FIG. 19. Profiles of the $^{23}Na$ concentration in OPC samples with w/c ratios of 0.3, 0.4 and 0.5 soaked in brine, showing enhanced uptake for larger w/c values. (reproduced from [98] with permission from Elsevier)

FIG. 20. Profiles of the ingress of $^{23}Na$ into an OPC sample as a function of soaking time. (reproduced from [98] with permission from Elsevier)

FIG. 21. 1-D profiles of the $^{27}Al$ content in cylindrical Secar 80® cement samples (reproduced from [98] with permission from Elsevier)

FIG. 22. (a) Raw and (b) deconvolved image of the $^{27}Al$ component in a Secar 80® cement sample, illustrating a 6 mm of the left side and a 8 mm hole on the right side. (reproduced from [98] with permission from Elsevier)

FIG. 23. Diffusion profiles of water into bentonite. (a) Diffusion of water from a reservoir (left hand side) into bentonite clay with initially 20 % w/b water. (b) Diffusion of water between two bentonite clay layers initially prepared $D_2O$ and $H_2O$ as indicated (reproduced from [90] with permission from Elsevier)

FIG. 24. Determination of the diffusion coefficients from the observed diffusion fronts shown in FIG. 23: (a) Diffusion along moisture gradient, (b) Self-diffusion

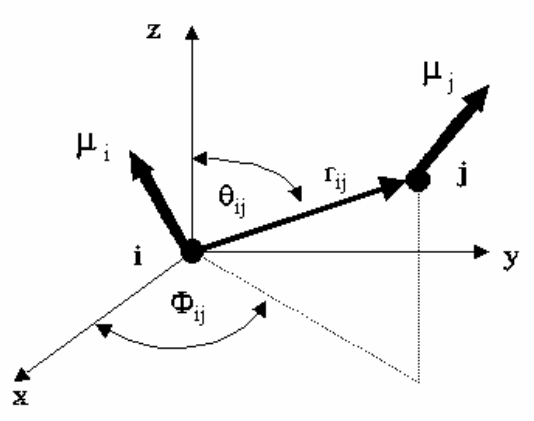


fig. 1

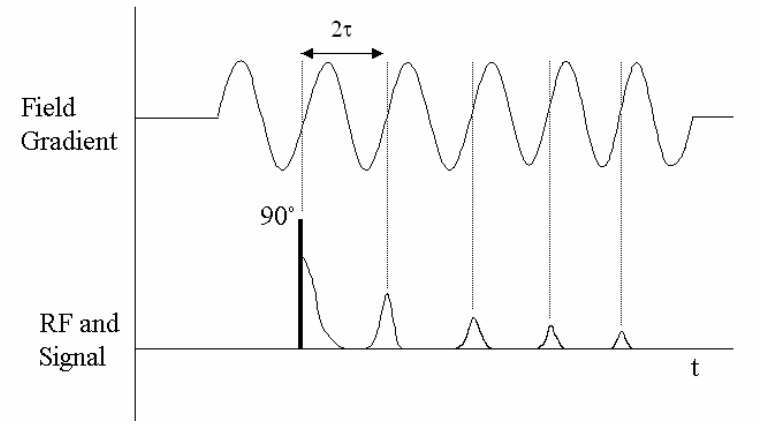


fig. 2

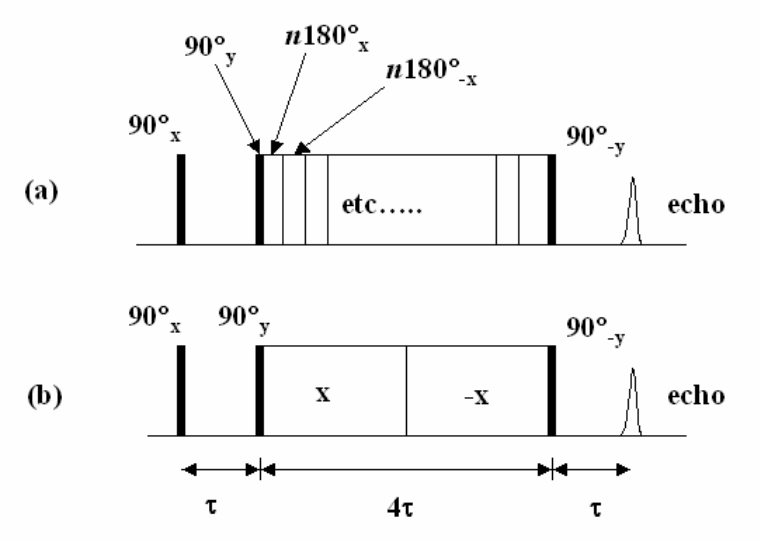


fig 3

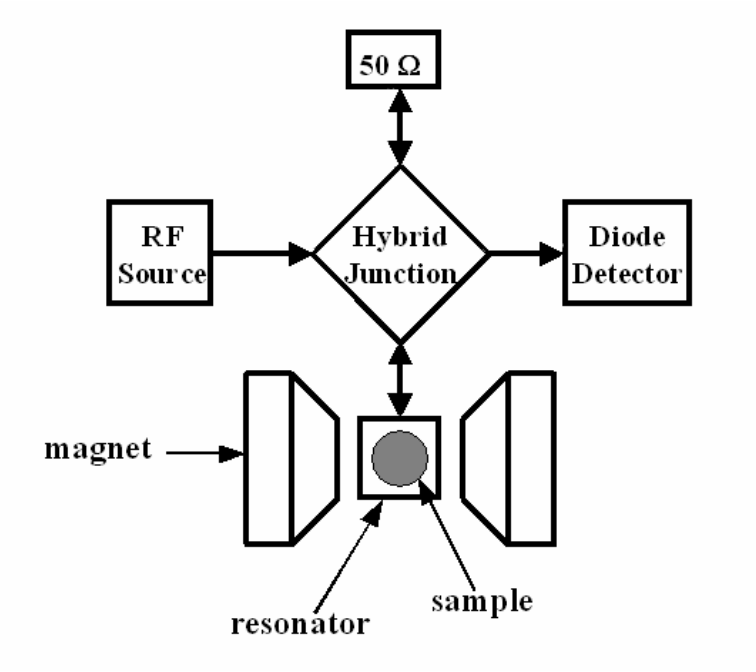
50 Ω
RF Source
Hybrid Junction
Diode Detector
magnet
resonator
sample

fig 4

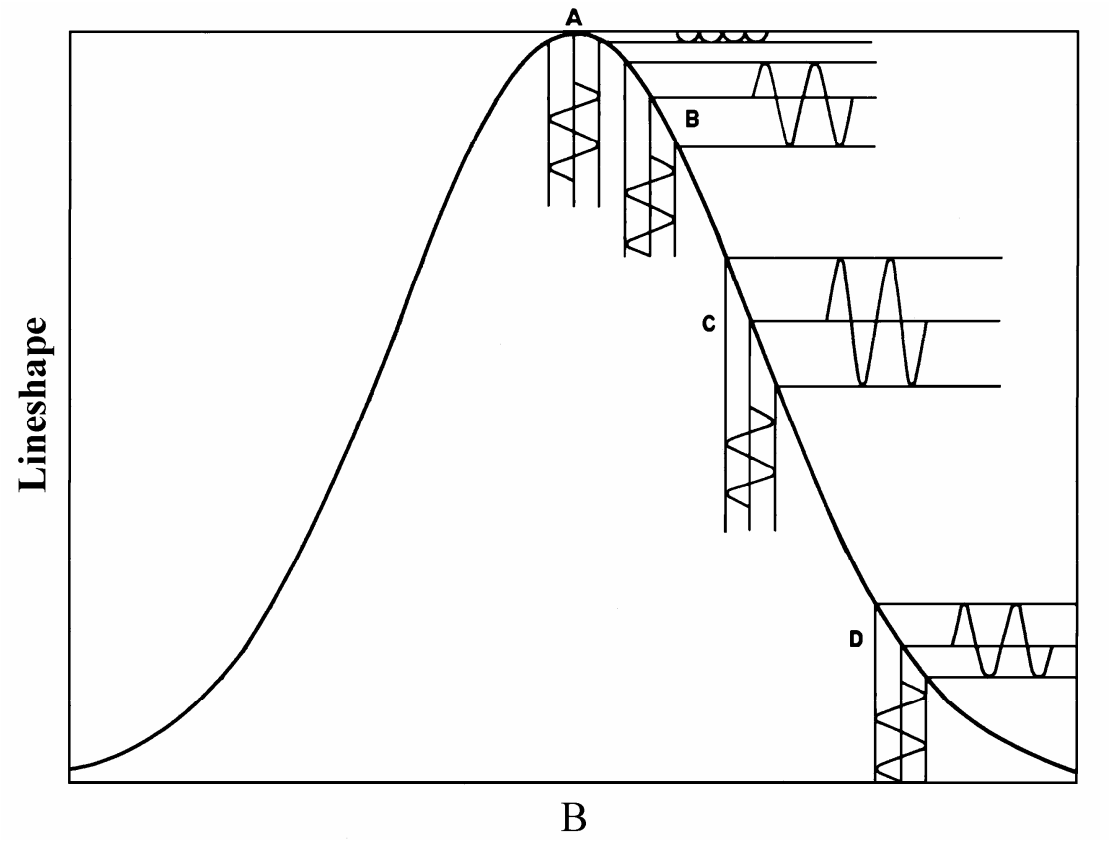


fig 5

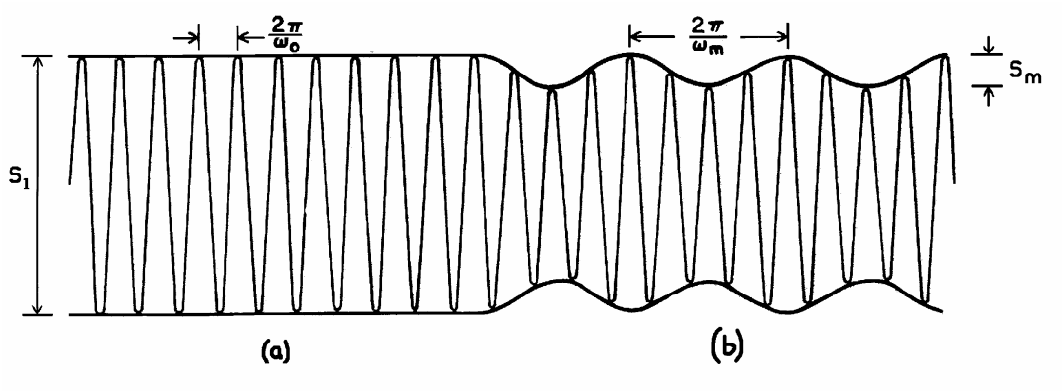


fig 6

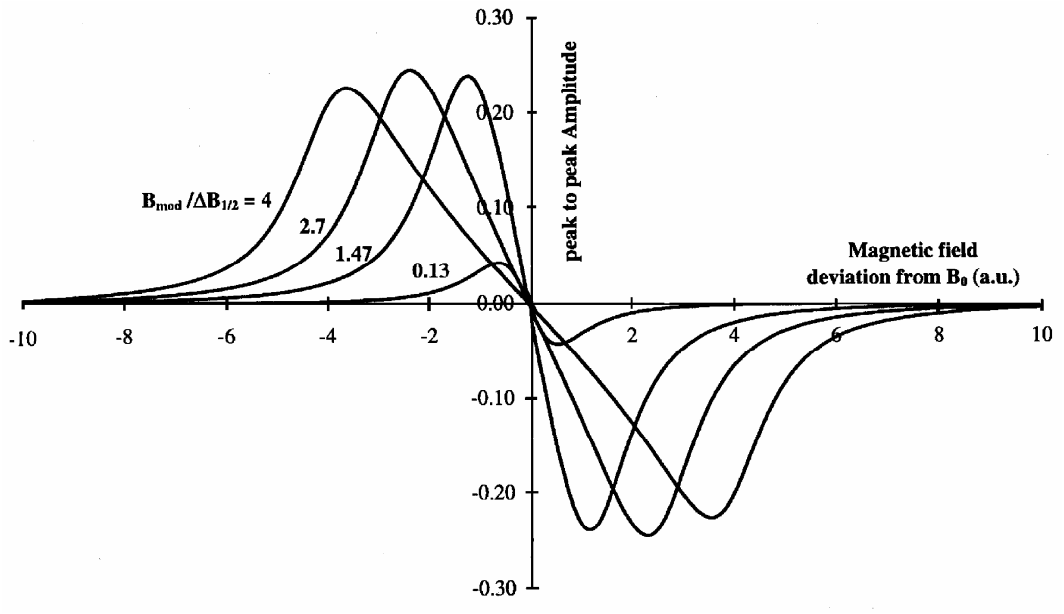
0.30
0.20
0.10
0.00
-0.10
-0.20
-0.30
-10
-8
-6
-4
-2
2
4
6
8
10
peak to peak Amplitude
Magnetic field
deviation from B0 (a.u.)
Bmod /ΔB1/2 = 4
2.7
1.47
0.13

fig 7

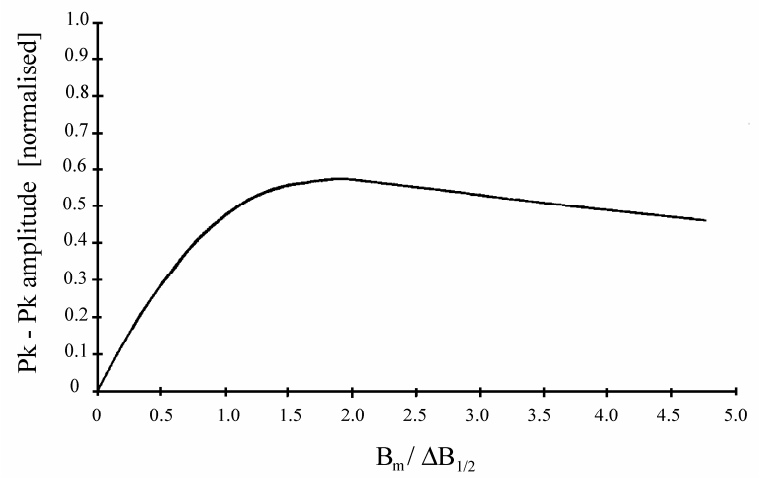
Pk - Pk amplitude [normalised]
1.0
0.9
0.8
0.7
0.6
0.5
0.4
0.3
0.2
0.1
0
0
0.5
1.0
1.5
2.0
2.5
3.0
3.5
4.0
4.5
5.0
$B_m / \Delta B_{1/2}$

fig 8

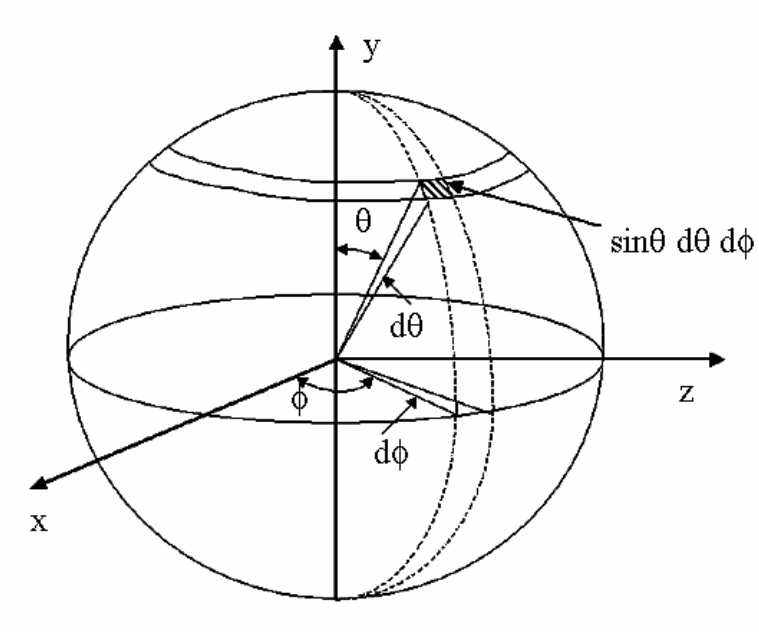


fig 9

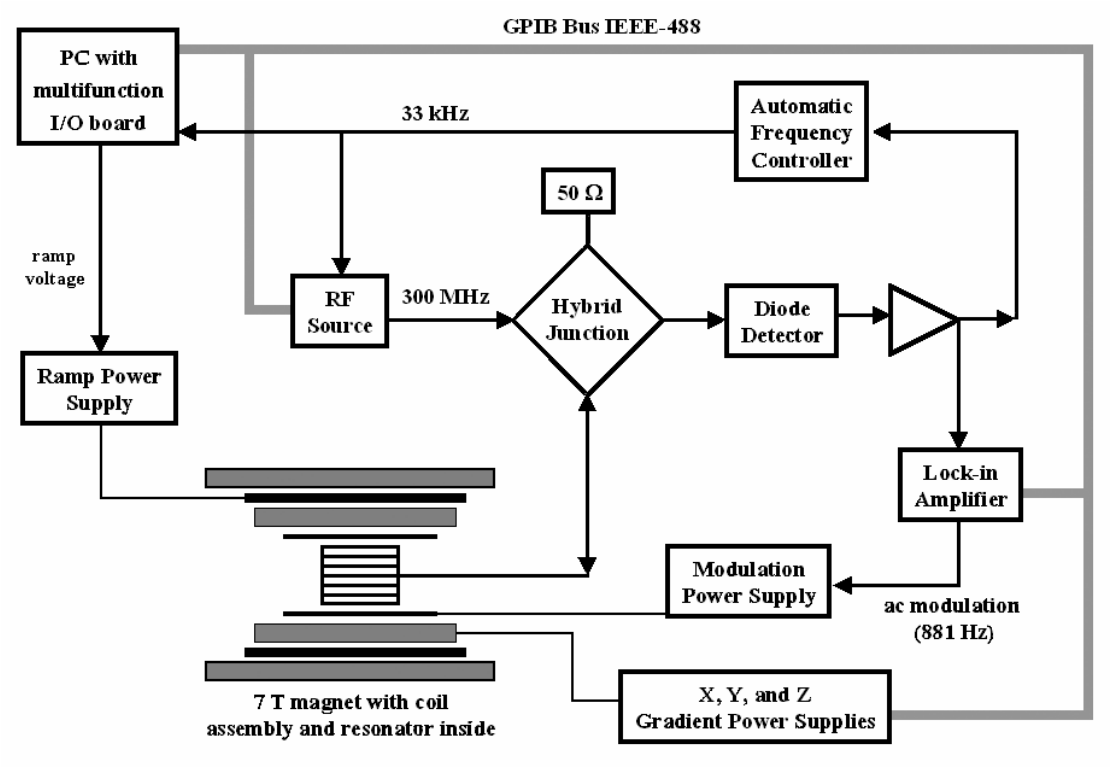
GPIB Bus IEEE-488
PC with multifunction I/O board
33 kHz
Automatic Frequency Controller
50 Ω
ramp voltage
RF Source
300 MHz
Hybrid Junction
Diode Detector
Ramp Power Supply
Lock-in Amplifier
Modulation Power Supply
ac modulation (881 Hz)
7 T magnet with coil assembly and resonator inside
X, Y, and Z Gradient Power Supplies

fig 10

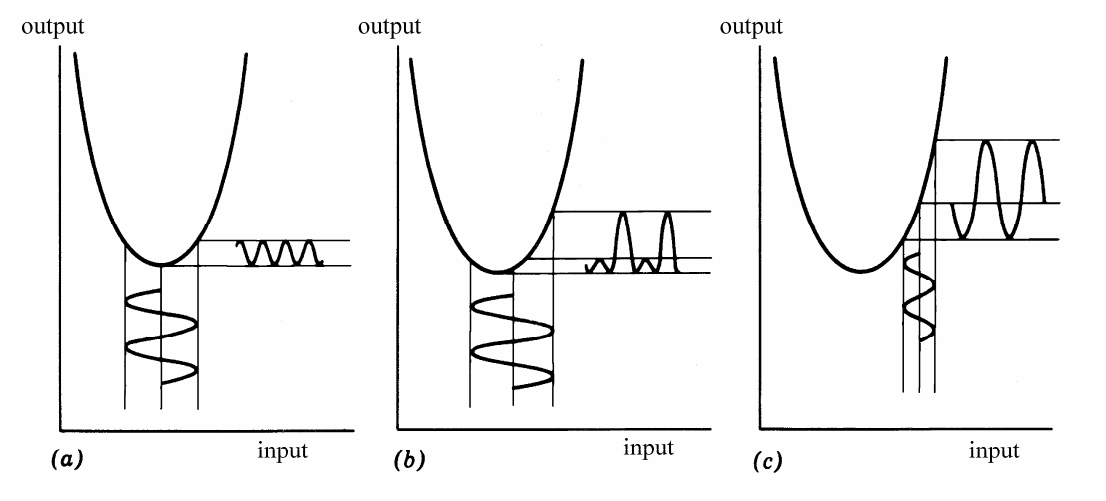


fig 11

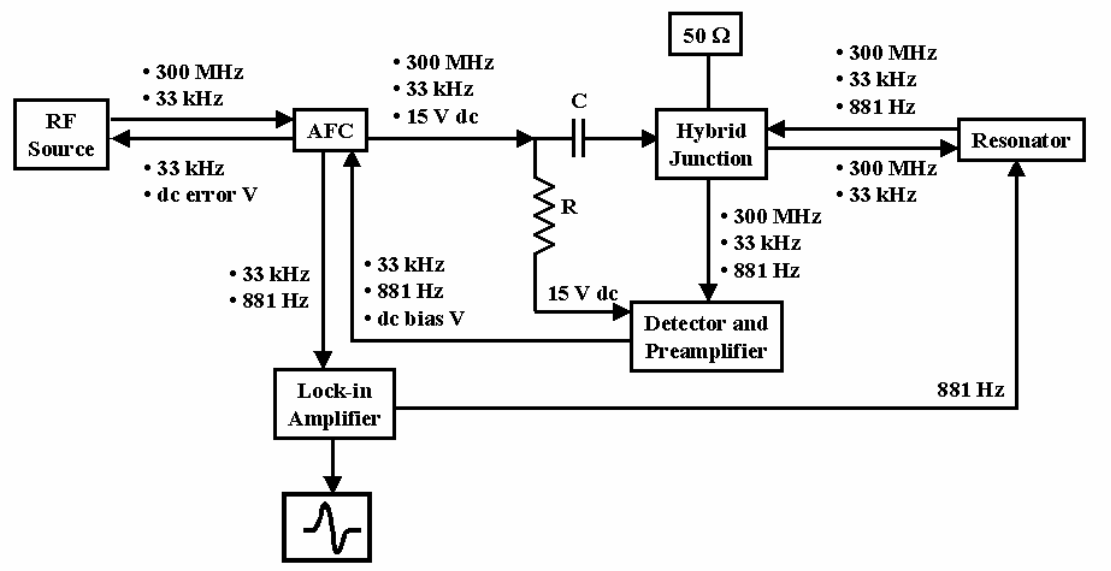
50 Ω
• 300 MHz
• 33 kHz
• 881 Hz
• 300 MHz
• 33 kHz
• 15 V dc
C
RF Source
AFC
Hybrid Junction
Resonator
• 300 MHz
• 33 kHz
• 881 Hz
• 33 kHz
• dc error V
• 300 MHz
• 33 kHz
R
• 300 MHz
• 33 kHz
• 881 Hz
• 33 kHz
• 881 Hz
• 33 kHz
• 881 Hz
• dc bias V
15 V dc
Detector and Preamplifier
Lock-in Amplifier
881 Hz

fig 12

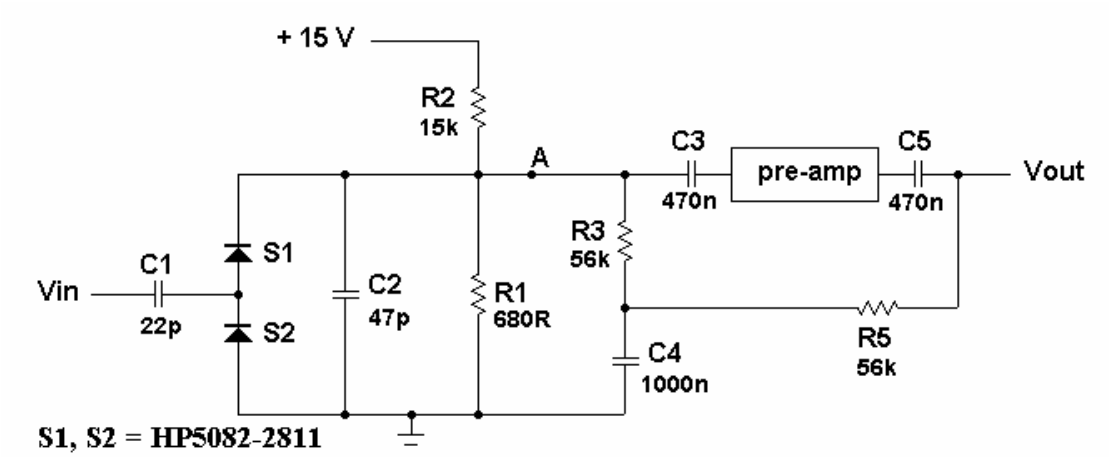
+ 15 V
R2
15k
A
C3
470n
pre-amp
C5
470n
Vout
R3
56k
C1
22p
Vin
S1
S2
C2
47p
R1
680R
C4
1000n
R5
56k
S1, S2 = HP5082-2811

fig 13

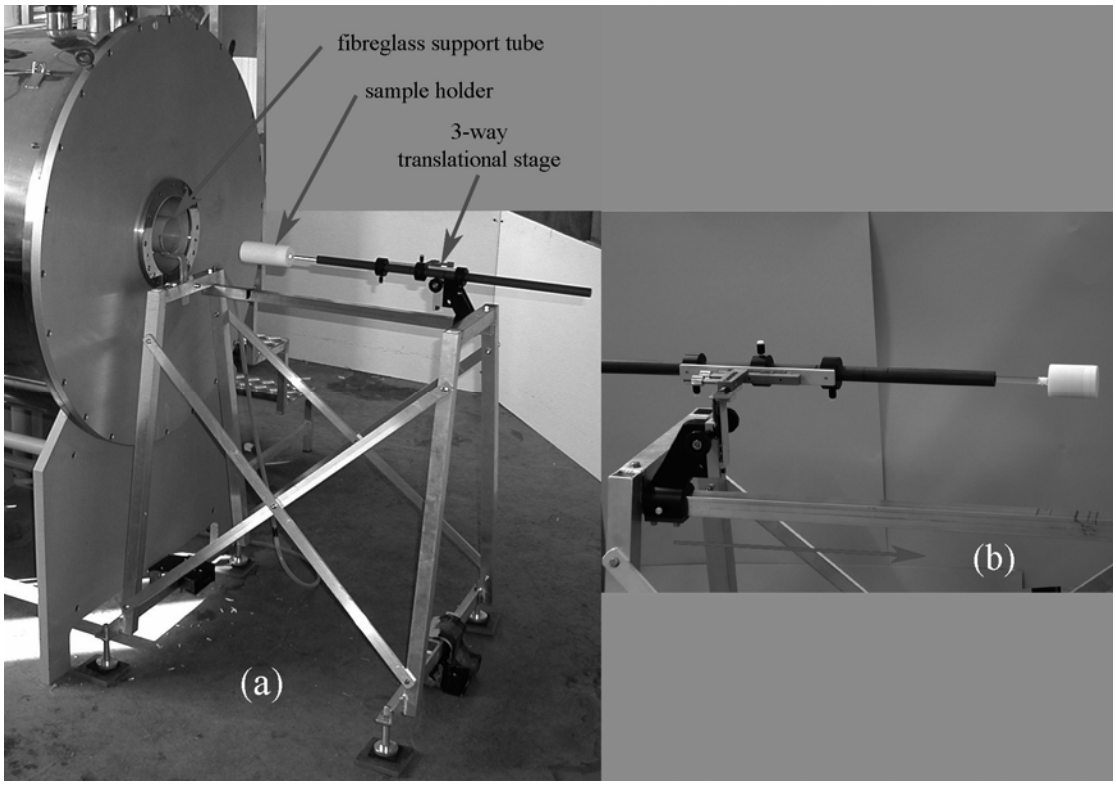
fibreglass support tube
sample holder
3-way
translational stage
(a)
(b)

fig 14

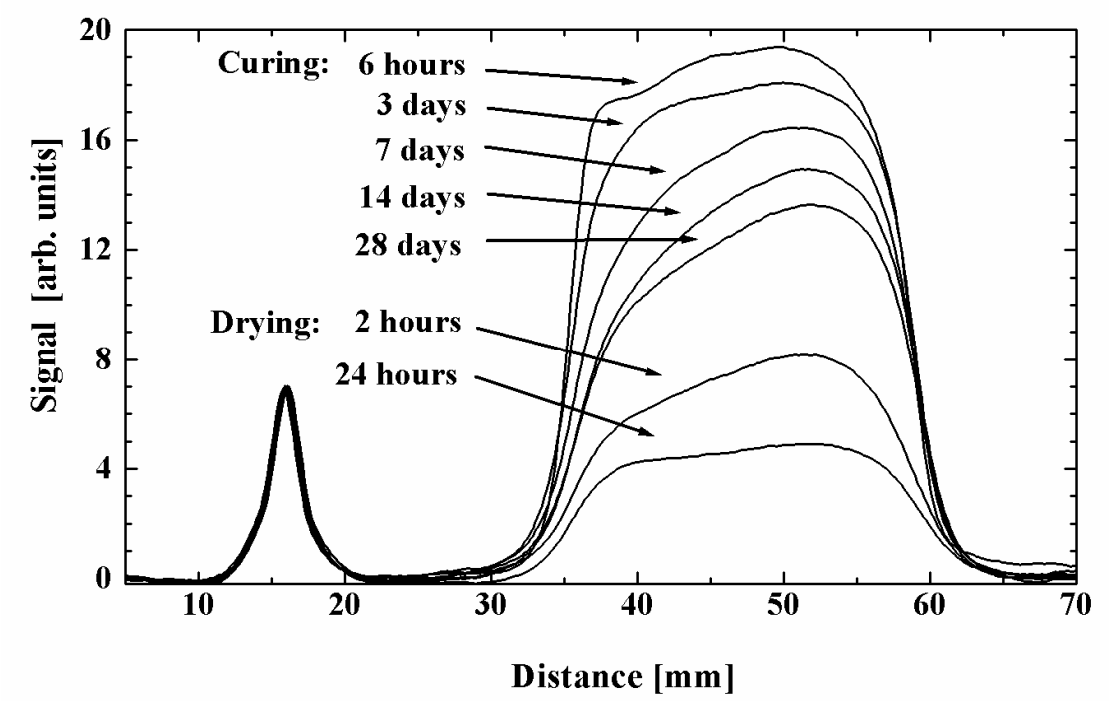
Curing:
6 hours
3 days
7 days
14 days
28 days
Drying:
2 hours
24 hours
Signal [arb. units]
Distance [mm]
0
4
8
12
16
20
10
20
30
40
50
60
70

fig 15

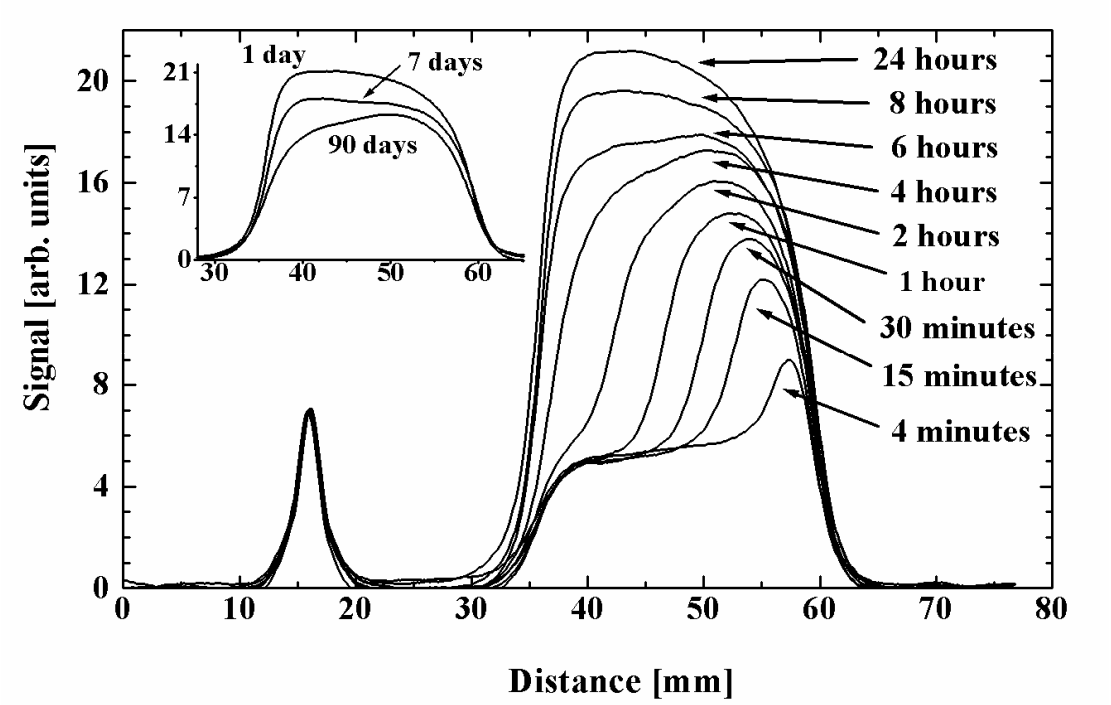
Signal [arb. units]
Distance [mm]
0
4
8
12
16
20
0
10
20
30
40
50
60
70
80
24 hours
8 hours
6 hours
4 hours
2 hours
1 hour
30 minutes
15 minutes
4 minutes
1 day
7 days
90 days
21
14
7
0
30
40
50
60

fig 16

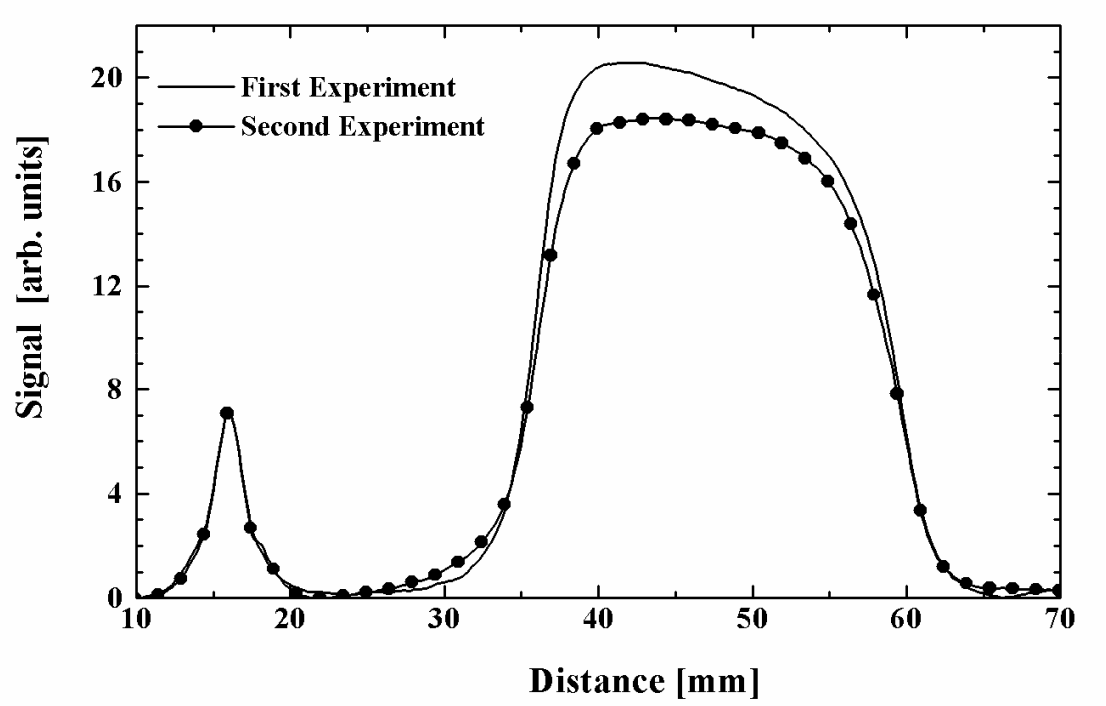
First Experiment
Second Experiment
Signal [arb. units]
Distance [mm]
0
4
8
12
16
20
10
20
30
40
50
60
70

fig 17

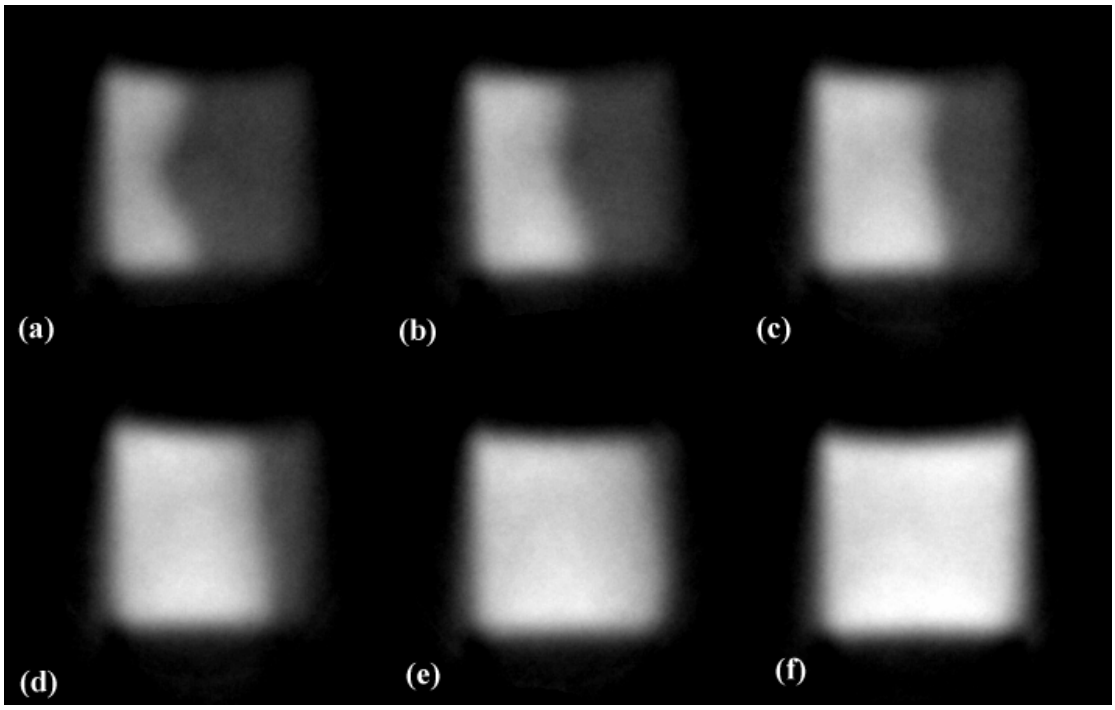


fig 18

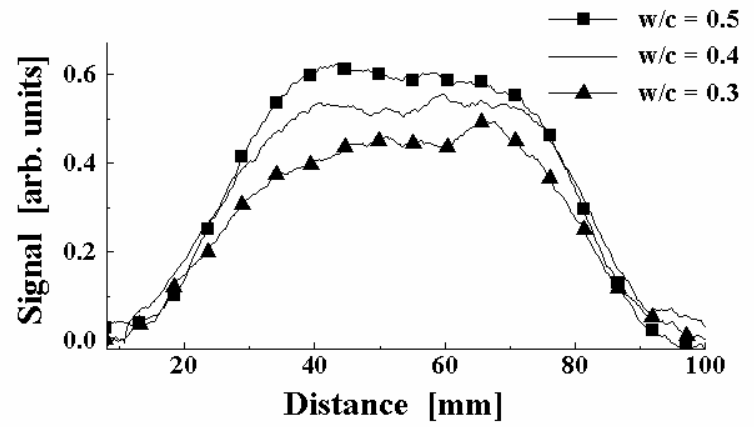
w/c = 0.5
w/c = 0.4
w/c = 0.3
Signal [arb. units]
0.0
0.2
0.4
0.6
20
40
60
80
100
Distance [mm]

fig 19

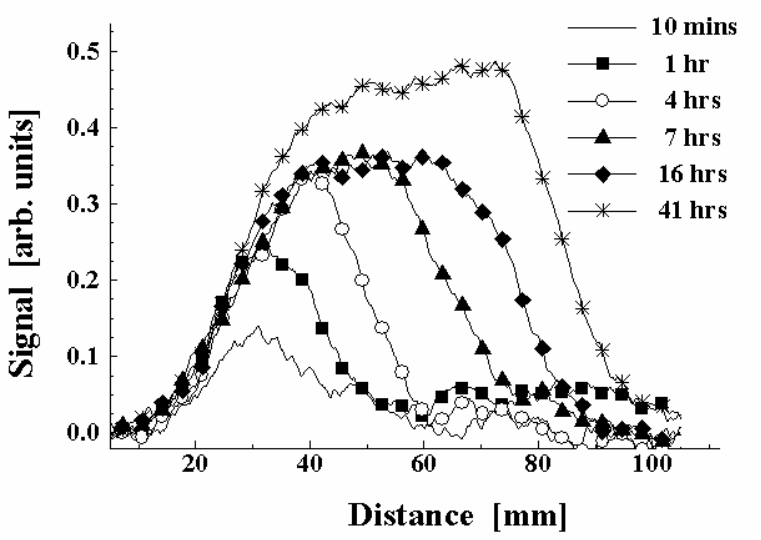
10 mins
1 hr
4 hrs
7 hrs
16 hrs
41 hrs
Signal [arb. units]
0.0
0.1
0.2
0.3
0.4
0.5
20
40
60
80
100
Distance [mm]

fig 20

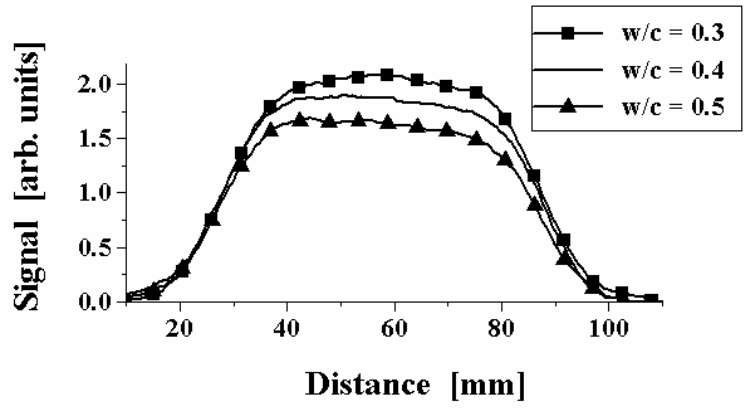
w/c = 0.3
w/c = 0.4
w/c = 0.5
Signal [arb. units]
2.0
1.5
1.0
0.5
0.0
20
40
60
80
100
Distance [mm]

fig 21

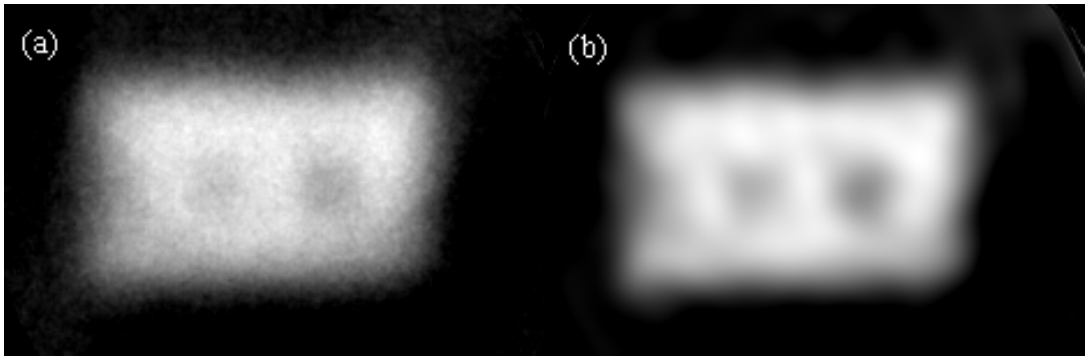


fig 22

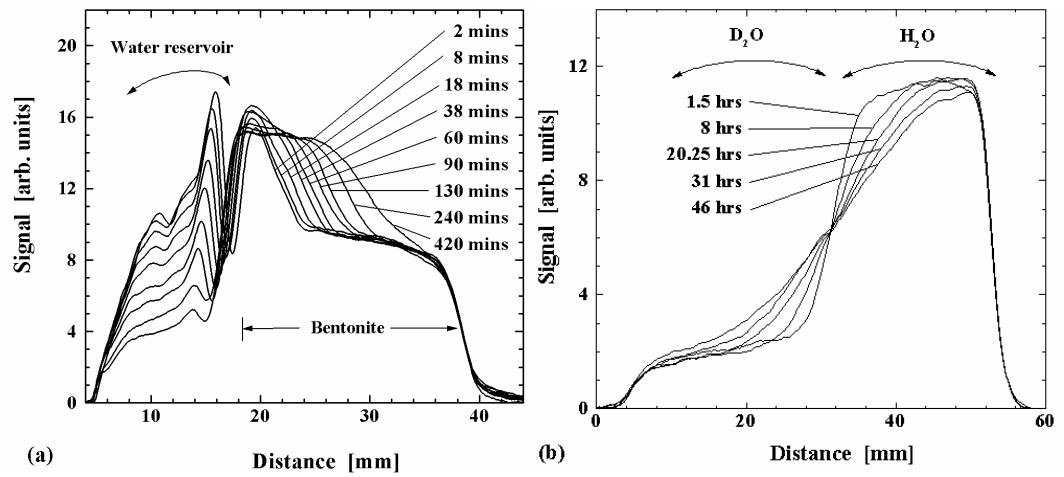
Water reservoir
2 mins
8 mins
18 mins
38 mins
60 mins
90 mins
130 mins
240 mins
420 mins
Bentonite
Signal [arb. units]
Distance [mm]
(a)
D2O
H2O
1.5 hrs
8 hrs
20.25 hrs
31 hrs
46 hrs
Signal [arb. units]
Distance [mm]
(b)

fig 23

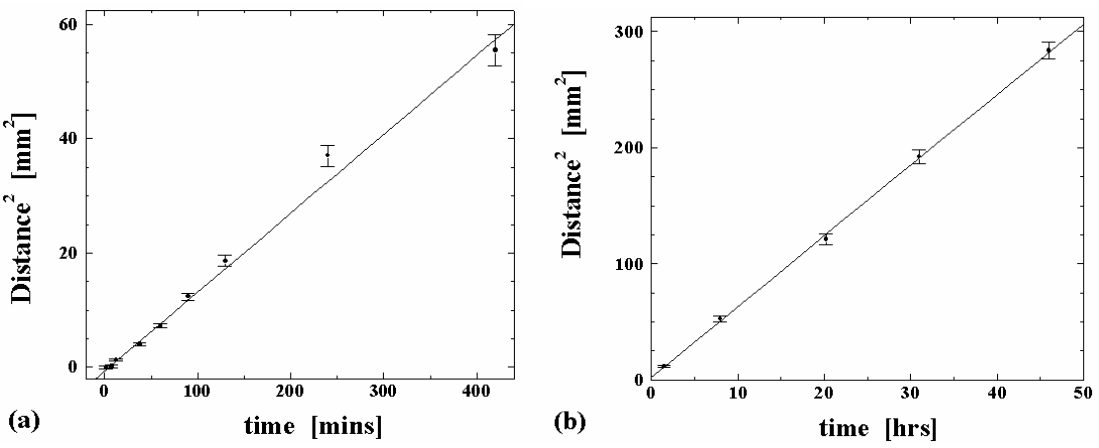
Distance$^2$ [mm$^2$]
60
40
20
0
0
100
200
300
400
time [mins]
(a)
Distance$^2$ [mm$^2$]
300
200
100
0
0
10
20
30
40
50
time [hrs]
(b)

fig 24

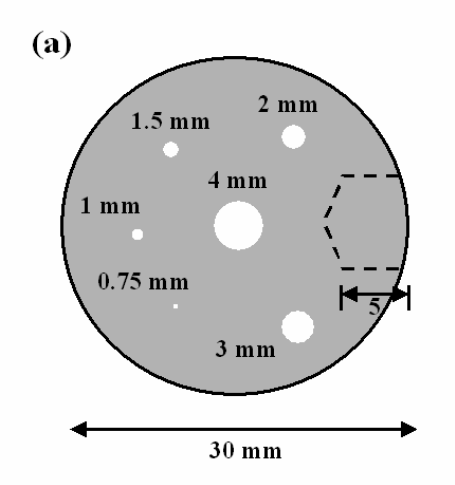


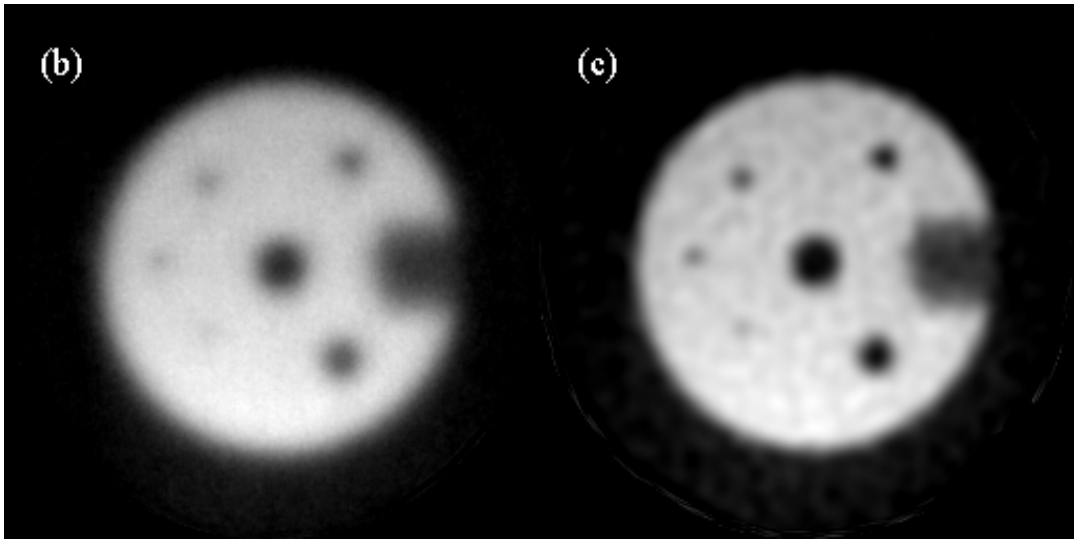


fig 25

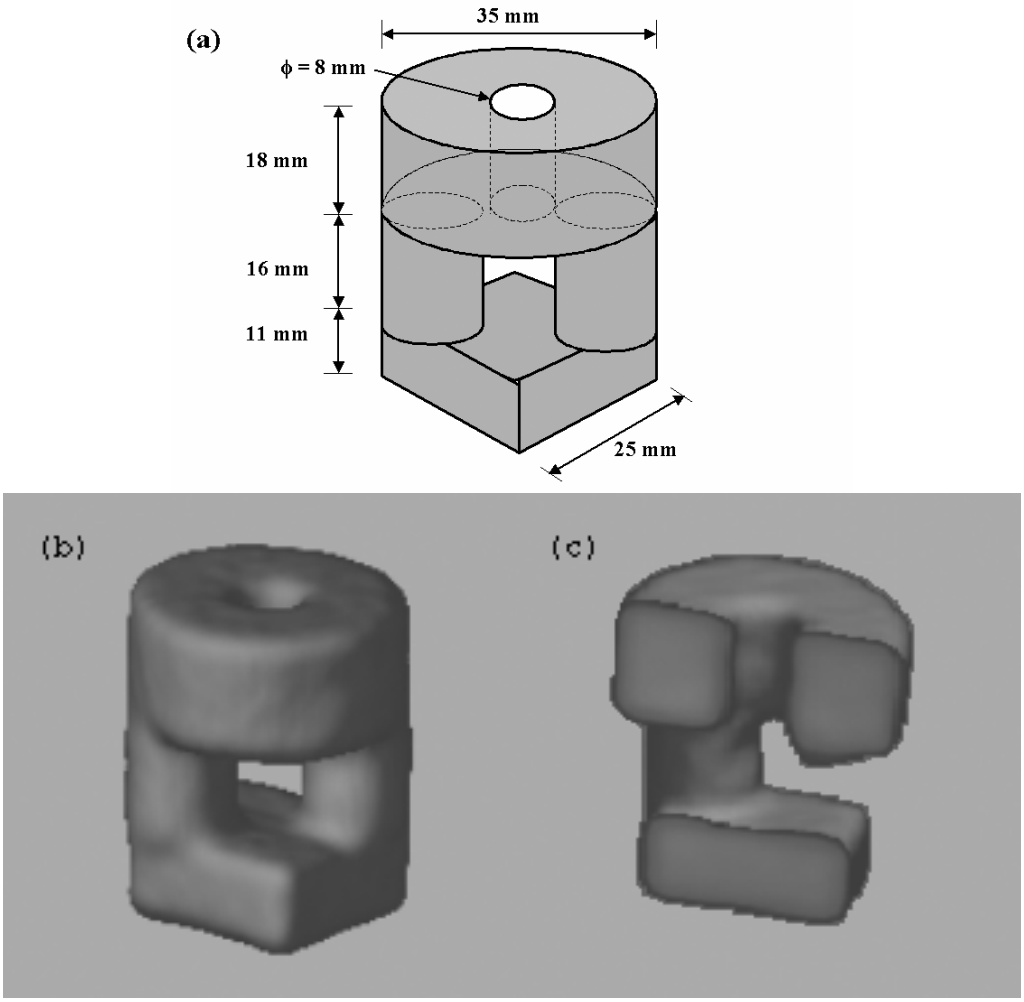


fig 26

TABLE 1

**Physical characteristics of the coil assembly**

| ***Parameter*** | ***Modulation*** | ***Ramp*** | ***X Gradient*** | ***Y Gradient*** | ***Z Gradient*** |
|---|---|---|---|---|---|
| No. Layers | 1 | 2 | 2 | 2 | 2 |
| No. Turns | 20 | 225 | - | - | 152 |
| Av. Radius [mm] | 49 | 73.3 | 50.8 | 53.4 | 69.5 |
| Thickness [mm] | 1 | 3.9 | 2 | 2 | 3.9 |
| Current [A] | 3.4 | 11.8 | 86 | 92 | 33.4 |
| Ohmic Voltage [V] | 0.7 | 7.2 | 5.6 | 6.0 | 13.9 |
| Resistance @ 25°C | 0.178 | 0.525 | 0.056 | 0.056 | 0.356 |
| Ohmic Power [W] | 2 | 85 | 482 | 552 | 464 |
| Inductance [μH] | 13 | - | - | - | - |
| Max. Field [mT] | ± 0.4 | ± 16 | - | - | - |
| Max. Gradient [mT/m] | - | - | 300 | 300 | 300 |
| Wire Length [m] | 6.2 | 103.6 | - | - | 66.4 |
| Calibration Factor [mT/m/A] or [mT/A] | 0.0706 | 0.8841 | 3.53 | 3.28 | 9.34 |
| Efficiency x $10^{-7}$/radius [$Tm^{-1}A^{-1}$] (see [99]) | - | - | 91.1 | 93.5 | 451 |